ACOUSTIC INVESTIGATIONS ON BENZOIC ACID IN WATER + METHANOL MIXTURES IN THE TEMPERATURE RANGE 293.15 TO 313.15 K

H. R. Shivakumar[1], Surekha M.and Siju[2], N. Antony[3]

[1,2]Department of Chemistry KVG College of Engineering, Sullia, D.K
[3]Department of Basic Science and Humanities, New Horizon College of Engineering, Bangalore, Affiliated to Visvesvaraya Technological University, Belgaum, Karnataka(India)

ABSTRACT

Ultrasonic velocity (U) and density (d) has been measured for Benzoic acid in various water + methanol systems at different temperatures. Using the experimental data, adiabatic compressibility (β_{ad}), apparent molar compressibility (Φ_K), limiting molar compressibility (Φ_k°), intermolecular free length (L_f,) specific acoustic impedance (Z), relative association (R_A), solvation number (S_n) are calculated and interpreted in terms of solute-solvent and solute co-solvent interactions.

Keywords: Benzoic Acid, Ion Solvation, Methanol, Solvation Number, Ultrasonic Velocity

I.INTRODUCTION

Ultrasonic velocity measurement technique has been found to be one of the most powerful tools in the investigation of structure and molecular interactions occurring in solutions. Electrolytes are expected to influence solvent structure, and these structural changes of the solvent causes variation in thermodynamic properties of solutions [1-10]. Ultrasonic waves, in recent years have acquired the status of an important probe for the study of structure and properties of matter. Various types of interactions exist in solutions viz. solute-solute, solute-solvent and solvent-solvent interactions. These interactions attracted current interest in all branches of chemistry since they provide a better understanding of how the solute modifies or distorts the structure of the solvent [11]. The present work is an attempt to explore the molecular interactions present in the ternary system of Benzoic acid + methanol + water at 293.15K, 303.15K, 308.15K and 313.15K by ultrasonic method. From the experimentally determined ultrasonic velocity (U) and density (d) various useful ultrasonic parameters and apparent molar volume (Φ_v) were determined.

II. EXPERIMENTAL

Benzoic acid (Merck, AR Grade) was dried at 100-120°C for three hours and stored in a vacuum desiccator. Triply distilled water (specific conductance $1x10^{-6}$ mho cm^{-1}) and purified methanol were used. Benzoic acid solution (0.1M) in water and various compositions of water-methanol (v/v) mixtures were prepared and diluted further to obtain the solutions of required concentrations. Ultrasonic velocity of these electrolytic solutions were measured using a digital ultrasonic interferometer (M-81, Mittal Enterprises, New Delhi)

at 2MHz with a measuring frequency tolerance ±0.01°C. Accuracy of the ultrasonic interferometer was examined with triply distilled water. A digital constant temperature bath (Kumar and Kumar, Mumbai) was used to circulate water through the double walled ultrasonic measuring cell made of steel containing the experimental solution at the desired temperature. The accuracy of temperature measured was ± 0.01K). Densities of all solutions were determined by using a pyknometer of 10cc capacity.

III.THEORY

Ultrasonic velocity, various acoustic and thermodynamic parameters like adiabatic compressibility (β_{ad}), intermolecular free length (L_f), specific acoustic impedance (Z), relative association (R_A), apparent molar compressibility (Φ_k), apparent molar volume (Φ_v) and solvation number (S_n) were calculated using the following equations [12]:

$$U = \lambda \times F \quad (1)$$

$$\beta_{ad} = 1/U^2 d \quad (2)$$

$$L_f = K\sqrt{\beta_{ad}} \quad (3)$$

$$Z = U \times d \quad (4)$$

$$R_A = (d/d_0)(U_0/U)^{1/3} \quad (5)$$

$$\Phi_k = 1000(d_0 \beta_{ad} - d_1 \beta^0_{ad}) / C d_0 + M \beta_{ad} / d_1 \quad (6)$$

$$\Phi_v = M/d_0 - 1000(d - d_0)/Cd_0 \quad (7)$$

$$S_n = (n_1/n_2)(1 - \beta_{ad}/\beta^0_{ad}) \quad (8)$$

where d_1, d_0 and U, U_0 are the densities and ultrasonic velocities of solution and solvent respectively. λ is the wavelength and F is the frequency of ultrasonic wave. M is the molecular weight of the solute, β^0_{ad} and β_{ad} are the adiabatic compressibility's of solvent and solution, C is the concentration, K is the Jacobson constant, n_1 and n_2 are the number of moles of the solvent and solute respectively.

IV. RESULTS AND DISCUSSION

The experimentally determined ultrasonic velocities (U) of Benzoic acid in different compositions of methanol + water at 293.15K, 303.15K, 308.15K and 313.15K are shown in TABLE 1. Ultrasonic velocity of Benzoic acid increased with increasing concentration of methanol up to 40%, further it decreased with further increase in methanol concentration. Density (TABLE 2) of benzoic acid in methanol + water mixtures increases with the increase in concentration. The existence of molecular interactions between solute and solvent molecules is responsible for the observed increase in ultrasonic velocity and density of these mixtures [11]. The above observations may be attributed to the cohesion brought about by ionic hydration [12, 13].

Adiabatic compressibility (β_{ad}) represents the magnitude of compressibility of a solvent in the presence of a solute without affecting the enthalpy of the system. Calculated values of adiabatic compressibility (β_{ad}) for benzoic acid in various compositions of the solvent mixture are shown in TABLE 1. The value of β_{ad} in benzoic acid systems shows a decreasing trend till 40% methanol and thereafter it increase with increase in methanol content. This type of observation is reported elsewhere [13], and it is attributed to solvent-solvent interactions and clathrate-like structure formation in the solvent mixtures. The increasing electrostrictive compression of water around the molecules results in a larger decrease in the compressibility of the solutions. Thus β_{ad} decreases

with increase in concentration. Adiabatic compressibility decreases [14, 15] for aqueous solutions with rise in temperature and the opposite trend is seen when co-solvent is present in significant proportions. This is due to opposing trends in their temperature coefficients of ultrasound propagation.

Intermolecular free length (L_f) calculated using (3) is shown in the TABLE 1 and it is found to increase with increase in temperature. This clearly reveals that ion-solvent and solvent-solvent interactions become weaker at high temperatures. It could also be seen (TABLE 1) that the intermolecular free length (L_f) decreases with increase in the percentage of methanol up to 60% methanol content. This is in tune with the trend in compressibility values. The L_f values are found to decrease with increase in concentration indicating increased solute-solvent and solute-solute interactions. Increase in density (TABLE 2) with increase in concentration is due to the shrinkage in volume which in turn is a consequence of increased attractive interactions [16]. Gradual increase in the impedance (Z) with the increase of concentration and variation with increase of temperature shows that molecular interactions in aqueous methanol + water solution are associative [17]. This suggests increase in molecular packing in medium and it may further support strengthening of molecular interactions [18] due to the presence of hydrogen bonding in aqueous methanol solutions. In accordance with U values, the Z values are found to increase with increase in temperature upto 20% solution of methanol in water and decrease with increase in temperature for other compositions. There is no significant variation in Relative association (R_A) with increase in temperature for Benzoic acid in water + methanol mixtures.

Limiting apparent molar compressibility (ϕ_k^0) was found out from the plot of ϕ_k against square root of concentration. The large negative values of ϕ_k may indicate the presence of packing effect [19] .The slope (S_k) of this plot and ϕ_k^0values are shown in the TABLE 3. ϕ_k is found to decrease linearly with concentration. Negative values of ϕ_k^0 are interpreted in terms of loss of compressibility of solvent due to electrostrictive solvation and positive S_k values suggest increased ion-ion/solute-solute interaction with increase in concentration [20]. Limiting apparent molar volume (ϕ_V) was found out from the plot of ϕ_v against square root of concentration. The positive value of S^*_V indicates strong ion –ion interaction and negative values of S^*_V signify the presence of weak solute-solute interaction in the mixture. From TABLE 4 it is noticed that the values of solvation number are found to decrease with ultrasonic velocity and density of these mixtures [11]. These observations in these solutions may be attributed to the cohesion brought about by ionic hydration [12, 13].

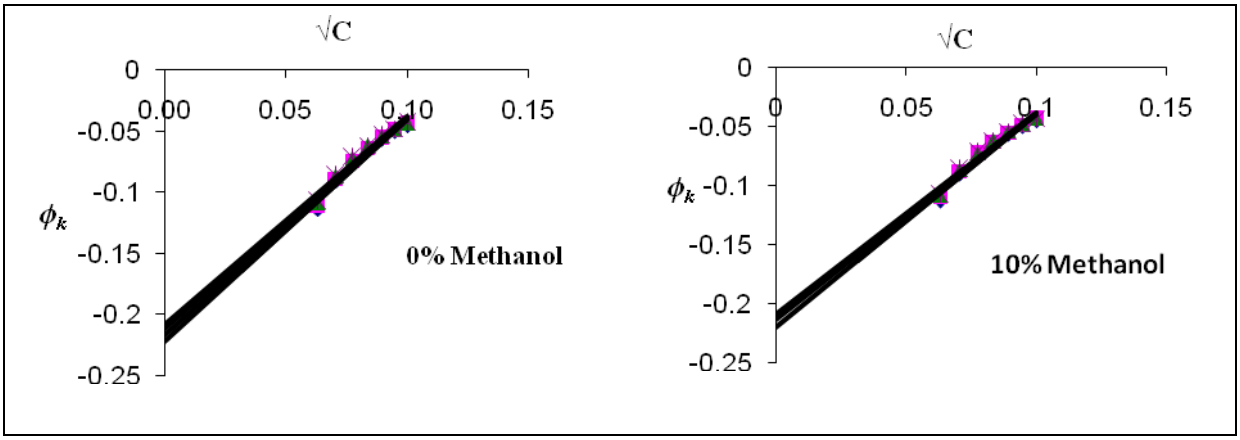

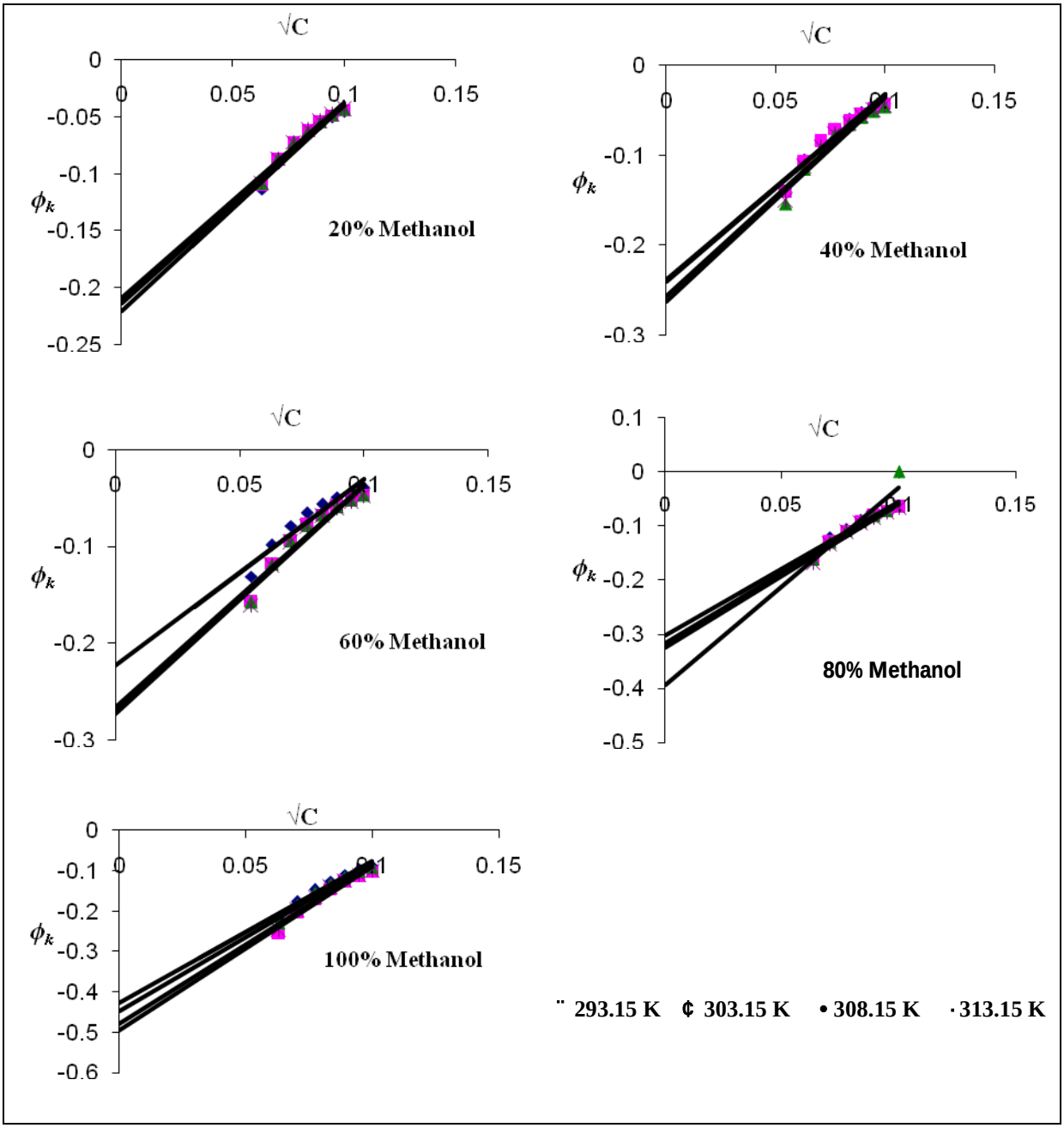

Figure 1 Plot of f_k (m^2 mol^{-1}) Vs √C ($mol^{1/2}$ $dm^{-3/2}$) for benzoic acid in methanol + water mixtures at different temperatures

TABLE 1

Computed Values Of Ultrasonic Velocity (U: M S-1), Adiabatic Compressibility (Bad: M2/N) And Intermolecular Free Length (Lf: M) With Respect To Concentration (C: Mol Dm-3) For Benzoic Acid In Methanol + Water Mixtures At Different Temperatures

C	TEMPERATURE

	293.15 K			303.15 K			308.15 K			313.15 K		
	U	$10^{10}\beta_{ad}$	$10^{10}L_f$	U	$10^{10}\beta_{ad}$	$10^{10}L_f$	U	$10^{10}\beta_{ad}$	$10^{10}L_f$	U	$10^{10}\beta_{ad}$	$10^{10}L_f$
0% Methanol												
0.001	1476	4.600	0.4191	1500	4.477	0.4222	1516	4.388	0.4213	1532	4.304	0.4212
0.002	1480	4.573	0.4179	1504	4.452	0.4210	1516	4.387	0.4212	1532	4.303	0.4211
0.003	1480	4.572	0.4178	1504	4.451	0.4210	1520	4.364	0.4201	1528	4.325	0.4222
0.004	1480	4.571	0.4178	1504	4.451	0.4210	1520	4.363	0.4201	1528	4.325	0.4222
0.005	1480	4.570	0.4177	1504	4.451	0.4209	1516	4.386	0.4212	1528	4.324	0.4221
0.006	1480	4.569	0.4177	1508	4.426	0.4198	1516	4.385	0.4211	1532	4.301	0.4210
0.007	1480	4.569	0.4177	1512	4.402	0.4186	1516	4.384	0.4211	1528	4.323	0.4221
0.008	1480	4.568	0.4177	1512	4.401	0.4186	1520	4.360	0.4199	1532	4.299	0.4209
0.009	1480	4.568	0.4176	1512	4.401	0.4186	1520	4.360	0.4199	1528	4.321	0.4220
0.010	1480	4.567	0.4176	1512	4.400	0.4185	1520	4.359	0.4199	1532	4.298	0.4209
10% Methanol												
0.001	1500	4.508	0.4148	1524	4.380	0.4176	1532	4.339	0.4189	1540	4.303	0.4211
0.002	1500	4.506	0.4137	1524	4.379	0.4175	1536	4.315	0.4178	1544	4.280	0.4200
0.003	1504	4.481	0.4125	1528	4.354	0.4164	1536	4.314	0.4177	1548	4.252	0.4186
0.004	1508	4.456	0.4114	1528	4.353	0.4163	1536	4.312	0.4176	1548	4.250	0.4186

0.005	1512	4.431	0.4113	1524	4.375	0.4174	1532	4.333	0.4187	1552	4.227	0.4174
0.006	1512	4.429	0.4112	1524	4.374	0.4173	1536	4.309	0.4175	1548	4.247	0.4184
0.007	1512	4.428	0.4090	1524	4.372	0.4172	1536	4.307	0.4174	1548	4.246	0.4183
0.008	1520	4.381	0.4090	1528	4.348	0.4161	1540	4.284	0.4163	1548	4.244	0.4183
0.009	1520	4.380	0.4089	1528	4.347	0.4160	1540	4.282	0.4162	1548	4.229	0.4175
0.010	1520	4.379	0.4089	1528	4.347	0.4160	1540	4.281	0.4161	1548	4.228	0.4175

20% Methanol

0.001	1532	4.326	0.4065	1548	4.257	0.4117	1544	4.286	0.4164	1548	4.275	0.4198
0.002	1532	4.326	0.4064	1548	4.256	0.4116	1548	4.262	0.4152	1548	4.274	0.4197
0.003	1532	4.324	0.4064	1548	4.254	0.4116	1548	4.260	0.4151	1552	4.251	0.4186
0.004	1536	4.300	0.4052	1548	4.253	0.4115	1548	4.259	0.4151	1556	4.227	0.4174
0.005	1540	4.277	0.4042	1552	4.229	0.4104	1556	4.214	0.4129	1552	4.248	0.4184
0.006	1544	4.254	0.4031	1552	4.228	0.4103	1556	4.213	0.4128	1564	4.181	0.4151
0.007	1544	4.253	0.4030	1548	4.227	0.4103	1556	4.212	0.4128	1564	4.181	0.4151
0.008	1548	4.230	0.4019	1552	4.226	0.4102	1556	4.210	0.4127	1564	4.179	0.4150
0.009	1548	4.229	0.4019	1552	4.226	0.4102	1560	4.188	0.4116	1564	4.178	0.4150
0.010	1548	4.228	0.4018	1552	4.225	0.4101	1560	4.187	0.4115	1564	4.177	0.4149

40% Methanol

0.001	1568	4.270	0.4038	1560	4.351	0.4162	1552	4.423	0.4230	1540	4.512	0.4313
0.002	1568	4.268	0.4038	1560	4.349	0.4161	1552	4.419	0.4228	1540	4.508	0.4270
0.003	1568	4.266	0.4036	1560	4.347	0.4160	1552	4.417	0.4227	1540	4.506	0.4269
0.004	1564	4.287	0.4036	1560	4.345	0.4159	1548	4.438	0.4237	1540	4.504	0.4268
0.005	1568	4.263	0.4035	1560	4.343	0.4158	1552	4.414	0.4225	1540	4.503	0.4268
0.006	1568	4.261	0.4034	1560	4.341	0.4157	1552	4.411	0.4224	1540	4.501	0.4267
0.007	1568	4.259	0.4033	1560	4.340	0.4157	1552	4.409	0.4223	1540	4.499	0.4266
0.008	1564	4.279	0.4043	1560	4.338	0.4156	1552	4.407	0.4222	1540	4.497	0.4265
0.009	1572	4.235	0.4022	1560	4.336	0.4155	1552	4.405	0.4221	1540	4.495	0.4264
0.010	1568	4.254	0.4031	1564	4.313	0.4144	1552	4.404	0.4221	1544	4.470	0.4252

60% Methanol

0.001	1484	4.935	0.4341	1472	5.070	0.4493	1452	5.256	0.4611	1440	5.363	0.4701
0.002	1480	4.958	0.4351	1472	5.068	0.4492	1452	5.254	0.4610	1434	5.406	0.4676
0.003	1484	4.930	0.4339	1472	5.065	0.4491	1452	5.252	0.4609	1440	5.358	0.4655
0.004	1484	4.928	0.4338	1472	5.064	0.4490	1452	5.251	0.4609	1440	5.355	0.4654

0.005	1484	4.925	0.4337	1472	5.061	0.4489	1448	5.277	0.4620	1439	5.360	0.4656
0.006	1484	4.924	0.4337	1468	5.087	0.4500	1448	5.275	0.4619	1440	5.351	0.4652
0.007	1484	4.922	0.4336	1468	5.085	0.4500	1448	5.273	0.4618	1439	5.356	0.4655
0.008	1484	4.920	0.4335	1468	5.081	0.4498	1448	5.270	0.4617	1439	5.356	0.4655
0.009	1484	4.918	0.4334	1464	5.108	0.4510	1444	5.297	0.4629	1439	5.353	0.4653
0.010	1484	4.914	0.4332	1456	5.161	0.4533	1444	5.294	0.4627	1439	5.351	0.4652

80% Methanol

0.001	1356	6.278	0.4897	1316	6.740	0.5181	1304	6.895	0.5281	1288	7.135	0.5423
0.002	1356	6.201	0.4866	1312	6.778	0.5195	1304	6.892	0.5238	1288	7.129	0.5328
0.003	1356	6.177	0.4857	1312	6.775	0.5194	1304	6.888	0.5237	1288	7.126	0.5327
0.004	1356	6.173	0.4856	1308	6.813	0.5208	1304	6.885	0.5236	1284	7.168	0.5342
0.005	1356	6.326	0.4915	1308	6.809	0.5207	1304	6.879	0.5234	1284	7.165	0.5341
0.006	1344	6.279	0.4897	1308	6.806	0.5206	1304	6.876	0.5232	1284	7.162	0.5340
0.007	1340	6.313	0.4910	1312	6.763	0.5189	1304	6.872	0.5231	1284	7.160	0.5339
0.008	1340	6.311	0.4909	1312	6.759	0.5188	1304	6.870	0.5230	1280	7.201	0.5355
0.009	1340	6.308	0.4908	1312	6.755	0.5186	1300	6.907	0.5244	1280	7.198	0.5354
0.010	1340	6.305	0.4907	1312	6.750	0.5184	1300	6.905	0.5243	1280	7.194	0.5352

100% Methanol												
0.001	1144	9.584	0.6050	1096	10.554	0.6482	1084	10.849	0.6625	1064	11.302	0.6825
0.002	1144	9.578	0.6048	1096	10.550	0.6481	1080	10.925	0.6595	1064	11.295	0.6706
0.003	1140	9.640	0.6068	1092	10.622	0.6503	1080	10.923	0.6595	1064	11.292	0.6705
0.004	1140	9.635	0.6066	1092	10.617	0.6502	1080	10.917	0.6593	1064	11.284	0.6703
0.005	1140	9.632	0.6065	1092	10.613	0.6501	1076	10.993	0.6616	1064	11.278	0.6701
0.006	1132	9.763	0.6106	1088	10.685	0.6522	1076	10.990	0.6615	1060	11.357	0.6725
0.007	1132	9.759	0.6105	1088	10.680	0.6521	1076	10.986	0.6614	1060	11.351	0.6723
0.008	1132	9.755	0.6104	1088	10.677	0.6520	1068	11.143	0.6661	1060	11.348	0.6722
0.009	1132	9.748	0.6102	1084	10.752	0.6543	1068	11.139	0.6660	1060	11.342	0.6720
0.010	1132	9.745	0.6101	1084	10.746	0.6541	1068	11.132	0.6657	1060	11.335	0.6718

TABLE 2

Computed values of density (d: kg m^{-3}), specific acoustic impedance (Z: kg m^{-2} s^{-1}) and relative association (R_A) with respect to concentration (C: mol dm^{-3}) for benzoic acid in methanol + water mixtures at different temperatures

C	TEMPERATURE											
	293.15 K			303.15 K			308.15 K			313.15 K		
	10^{-3}d	10^{-5} Z	R_A	10^{-3}d	10^{-5} Z	R_A	10^{-3}d	10^{-5} Z	R_A	10^{-3}d	10^{-5} Z	R_A
0% Methanol												
0.001	0.9978	14.70	1.000	0.9926	14.9	0.999	0.9915	15.03	0.999	0.9898	15.16	0.998
0.002	0.9982	14.78	1.000	0.9928	14.9	0.998	0.9917	15.03	0.999	0.9900	15.16	0.998

0.003	0.9985	14.78	1.000	0.993	14.9	0.998	0.9918	15.07	0.998	0.9902	15.13	0.999
0.004	0.9987	14.78	1.000	0.9931	14.9	0.998	0.9919	15.04	0.998	0.9903	15.13	0.999
0.005	0.9989	14.78	1.000	0.9932	14.9	0.998	0.992	15.04	0.999	0.9904	15.13	0.999
0.006	0.9990	14.78	1.000	0.9934	14.9	0.998	0.9921	15.04	0.999	0.9906	15.17	0.998
0.007	0.9991	14.78	1.000	0.9935	15.0	0.997	0.9923	15.04	0.999	0.9907	15.13	0.999
0.008	0.9993	14.78	1.000	0.9937	15.0	0.997	0.9925	15.08	0.998	0.9909	15.18	0.998
0.009	0.9994	14.79	1.000	0.9938	15.0	0.997	0.9927	15.08	0.9990	0.9910	15.14	0.999
0.010	0.9995	14.79	1.000	0.9941	15.0	0.997	0.9928	15.09	0.999	0.9912	15.18	0.999
10% Methanol												
0.001	0.9860	14.80	0.998	0.9830	14.9	0.999	0.9820	15.04	0.999	0.9799	15.09	0.999
0.002	0.9863	14.80	0.998	0.9833	14.9	0.999	0.9823	15.08	0.998	0.9801	15.13	0.998
0.003	0.9866	14.80	0.997	0.9836	15.0	0.998	0.9826	15.09	0.998	0.9815	15.19	0.997
0.004	0.9869	14.90	0.996	0.9840	15.0	0.998	0.983	15.09	0.998	0.9818	15.19	0.998
0.005	0.9872	14.90	0.995	0.9842	15.0	0.999	0.9833	15.06	0.999	0.9822	15.24	0.997
0.006	0.9876	14.90	0.996	0.9844	15.0	0.999	0.9836	15.10	0.998	0.9826	15.21	0.998
0.007	0.9878	14.90	0.996	0.9847	15.0	1.000	0.9841	15.11	0.999	0.9829	15.21	0.998
0.008	0.988	15.00	0.994	0.985	15.0	0.999	0.9843	15.15	0.998	0.9832	15.21	0.998
0.009	0.9882	15.00	0.994	0.9853	15.0	0.999	0.9847	15.16	0.998	0.9868	15.27	0.999
0.010	0.9885	15.00	0.994	0.9854	15.0	0.999	0.9850	15.16	0.998	0.987	15.27	0.999
20% Methanol												
0.001	0.9848	15.08	1.009	0.9803	15.17	1.005	0.9788	15.11	1.012	0.9762	15.11	1.010
0.002	0.9850	15.09	1.009	0.9806	15.17	1.005	0.9791	15.15	1.011	0.9764	15.11	1.011
0.003	0.9854	14.61	1.009	0.981	15.18	1.005	0.9795	15.16	1.012	0.9767	15.16	1.010
0.004	0.9857	15.14	1.008	0.9812	15.18	1.005	0.9798	15.16	1.012	0.9771	15.20	1.009
0.005	0.9859	15.18	1.008	0.9816	15.23	1.004	0.9801	15.25	1.010	0.9774	15.17	1.010
0.006	0.9860	15.22	1.007	0.9819	15.24	1.004	0.9803	15.25	1.010	0.9777	15.29	1.008

0.007	0.9863	15.22	1.007	0.9872	15.28	1.007	0.9805	15.26	1.010	0.9779	15.29	1.008
0.008	0.9866	15.27	1.006	0.9823	15.24	1.004	0.981	15.26	1.010	0.9782	15.29	1.008
0.009	0.9868	15.28	1.006	0.9825	15.25	1.004	0.9812	15.30	1.010	0.9785	15.30	1.008
0.010	0.9871	15.28	1.006	0.9827	15.25	1.004	0.9815	15.31	1.010	0.9787	15.30	1.008
40% Methanol												
0.001	0.9525	14.93	0.999	0.9444	14.73	0.999	0.9387	14.56	1.011	0.9344	14.39	1.007
0.002	0.9529	14.94	0.999	0.9448	14.73	0.999	0.9396	14.58	1.012	0.9353	14.40	1.007
0.003	0.9534	14.94	0.999	0.9453	14.74	0.999	0.9400	14.58	1.012	0.9357	14.40	1.007
0.004	0.9536	14.91	1.000	0.9457	14.75	0.999	0.9404	14.55	1.013	0.9361	14.41	1.007
0.005	0.9540	14.95	1.000	0.9462	14.76	1.000	0.9406	14.59	1.012	0.9363	14.41	1.008
0.006	0.9546	14.96	1.000	0.9467	14.76	1.000	0.9411	14.60	1.012	0.9368	14.42	1.008
0.007	0.9549	14.97	1.000	0.9469	14.77	1.000	0.9415	14.61	1.012	0.9373	14.43	1.008
0.008	0.9553	14.94	1.001	0.9472	14.77	1.000	0.9420	14.61	1.013	0.9377	14.44	1.008
0.009	0.9556	15.02	0.999	0.9477	14.78	1.000	0.9424	14.62	1.013	0.9381	14.44	1.008
0.010	0.9560	14.99	1.000	0.9479	14.82	0.999	0.9427	14.63	1.013	0.9384	14.48	1.007
60% Methanol												
0.001	0.9202	13.65	1.010	0.9102	13.39	1.010	0.9024	13.10	1.010	0.8992	12.94	1.011
0.002	0.9208	13.62	1.011	0.9106	13.40	1.010	0.9028	13.10	1.010	0.8996	12.90	1.013
0.003	0.9211	13.66	1.010	0.9111	13.41	1.011	0.9030	13.11	1.010	0.9001	12.96	1.012
0.004	0.9215	13.67	1.010	0.9114	13.41	1.011	0.9033	13.11	1.010	0.9005	12.96	1.012
0.005	0.9219	13.68	1.010	0.9120	13.42	1.011	0.9038	13.08	1.011	0.9009	12.96	1.012
0.006	0.9222	13.68	1.010	0.9122	13.39	1.012	0.9041	13.09	1.012	0.9012	12.97	1.012
0.007	0.9225	13.69	1.010	0.9125	13.39	1.012	0.9045	13.09	1.012	0.9016	12.97	1.012
0.008	0.9230	13.69	1.011	0.9132	13.40	1.012	0.9050	13.10	1.012	0.9016	12.97	1.012
0.009	0.9233	13.70	1.011	0.9134	13.37	1.013	0.9054	13.07	1.013	0.9021	12.98	1.013
0.010	0.9240	13.71	1.011	0.9139	13.30	1.015	0.9059	13.08	1.013	0.9024	12.98	1.013
80% Methanol												

0.001	0.8663	11.74	0.990	0.8566	11.27	0.996	0.8529	11.12	0.990	0.8449	10.88	0.992
0.002	0.8771	11.89	0.994	0.8571	11.24	0.998	0.8534	11.12	0.990	0.8455	10.89	0.992
0.003	0.8805	11.93	0.995	0.8575	11.25	0.998	0.8538	11.13	0.991	0.8459	10.89	0.992
0.004	0.8809	11.94	0.995	0.8579	11.22	0.999	0.8542	11.13	0.991	0.8461	10.86	0.993
0.005	0.8813	11.65	0.987	0.8584	11.22	0.999	0.8549	11.14	0.991	0.8465	10.86	0.993
0.006	0.8817	11.85	0.998	0.8588	11.23	0.999	0.8552	11.15	0.991	0.8469	10.87	0.994
0.007	0.8821	11.82	1.000	0.8590	11.27	0.998	0.8558	11.15	0.991	0.8471	10.87	0.994
0.008	0.8825	11.82	1.000	0.8595	11.27	0.999	0.8560	11.16	0.991	0.8476	10.84	0.995
0.009	0.8829	11.83	1.000	0.8600	11.28	0.999	0.8567	11.13	0.993	0.8479	10.85	0.995
0.010	0.8833	11.83	1.000	0.8606	11.29	0.999	0.8569	11.14	0.993	0.8484	10.85	0.995
100% Methanol												
0.001	0.7973	9.12	0.975	0.7888	8.64	0.997	0.7844	8.5	0.976	0.7815	8.31	0.981
0.002	0.7977	9.12	0.975	0.7891	8.64	0.997	0.7848	8.47	0.978	0.7820	8.32	0.981
0.003	0.7982	9.09	0.976	0.7895	8.62	0.998	0.7849	8.47	0.978	0.7823	8.32	0.981
0.004	0.7986	9.1	0.977	0.7899	8.62	0.999	0.7853	8.48	0.978	0.7828	8.32	0.981
0.005	0.7989	9.1	0.977	0.7902	8.62	0.999	0.7857	8.45	0.979	0.7833	8.33	0.981
0.006	0.7993	9.04	0.979	0.7906	8.6	1.000	0.7859	8.45	0.979	0.7836	8.30	0.983
0.007	0.7997	9.05	0.979	0.7910	8.6	1.000	0.7862	8.45	0.980	0.7841	8.31	0.983
0.008	0.8000	9.05	0.979	0.7912	8.6	1.000	0.7868	8.4	0.982	0.7843	8.31	0.983
0.009	0.8005	9.06	0.980	0.7915	8.58	1.002	0.7871	8.4	0.982	0.7847	8.31	0.983
0.010	0.8008	9.06	0.980	0.7920	8.58	1.002	0.7876	8.41	0.983	0.7852	8.32	0.983

TABLE 3

Computed values of limiting apparent molar compressibility (f_k^0: m^2 mol^{-1}) and the associated slope (S_k) for benzoic acid in methanol + water mixtures at different temperatures

% of Methanol	TEMPERATURE			
	293.15 K	303.15 K	308.15 K	313.15 K

	$10^{15} f_k^0$	$10^{15} S_k$	$10^{15} f_k^0$	$10^{15} S_k$	$10^{15} f_k^0$	$10^{15} S_k$	$10^{15} f_k^0$	$10^{15} S_k$
0	-0.222	1.818	-0.215	1.723	-0.212	1.737	-0.209	1.713
10	-0.220	1.804	-0.213	1.747	-0.211	1.727	-0.209	1.709
20	-0.224	1.833	-0.216	1.723	-0.219	1.793	-0.210	1.725
40	-0.238	2.059	-0.240	2.073	-0.262	2.271	-0.255	2.21
60	-0.233	1.930	-0.266	2.297	-0.268	2.321	-0.273	2.359
80	-0.373	3.338	-0.389	3.478	-0.288	3.467	-0.400	3.579
100	-0.428	3.504	-0.495	4.052	-0.447	3.661	-0.480	3.933

TABLE4

Computed values of solvation number (S_n) for benzoic acid in methanol + water mixtures at different temperature

C	TEMPERATURE 293.15K	303.15K	308.15K 313.15K	
		0%		
0.001	-	-79.2	-84.0	197.7
0.002	8.5	113.7	-36.4	104.4
0.003	11.2	79.5	75.05	-23.3
0.004	11.2	61.0	57.68	-16.0
0.005	11.2	49.9	-11.19	-11.7
0.006	10.2	92.3	-8.39	40.40
0.007	9.6	121.4	-5.59	-5.9
0.008	9.7	107.6	33.0	32.3
0.009	9.3	96.2	30.59	-2.7
0.01	8.9	88.2	28.08	27.5
		10%		
0.001	484.0	253.1	1152.0	183.8
0.002	250.0	134.6	719.0	234.2
0.003	265.1	187.2	484.6	271.6
0.004	272.1	145.7	368.7	207.7
0.005	275.8	63.5	244.1	224.2
0.006	233.3	54.7	251.0	145.5
0.007	201.5	49.2	218.9	127.0
0.008	245.4	79.5	226.3	113.1
0.009	219.3	72.5	203.5	121.7

0.01	198.9	65.7	184.7	110.6
		20%		
0.001	1736.7	1446.2	1052.6	1553.3
0.002	873.3	730.6	661.9	781.6
0.003	588.8	493.7	448.0	610.4
0.004	508.9	372.8	339.7	525.4
0.005	459.5	352.9	375.9	373.2
0.006	425.5	296.5	314.9	437.8
0.007	366.8	255.8	271.4	376.7
0.008	353.8	224.9	240.5	331.4
0.009	315.6	201.0	242.7	296.2
0.01	285.4	181.9	219.9	267.6

V. CONCLUSIONS

The experimental values for ultrasonic velocity, density and viscosity of benzoic acid in different compositions of methanol in water have been determined at different temperatures. From the data, some acoustic parameters were calculated to explain the intermolecular interactions that occur between the solute and the solvent. Ultrasonic studies exposed strong solvent – solvent interactions prevailing in the solvent mixture of 40% methanol. It was observed that these strong solvent-solvent interactions significantly influenced various properties of the solutions.

VI. ACKNOWLEDGEMENTS

The authors are grateful to Visvesvaraya Technological University, Belgaum, India for the financial support under the grant Ref. No. VTU/Aca/2010-11/A-9/11329 dated 17th December 2010, and Dr. Renukaprasad K.V, General Secretary, AOLE Sullia, for the infrastructure and facilities.

REFERENCES

[1] Ishwara Bhat J , Shivakumar H.R., Conductometric studies on salvation behaviour of Tartaric acid in various solvent mixtures, *Journal of Molecular Liquids, 111*, ***2004***, *101- 108.*

[2] Ishwara Bhat J, Shivakumar H.R., Acoustic and solvation behaviour of potassium thiocyanate in mixed solvents .*Indian Journal of Pure & Applied Physics, 38,* ***2000*** *,306-312*

[3] Ishwara Bhat J Shivakumar H.R.,Study on Acoustic behaviour of Potassium thiocyanate in aqueous and various non aqueous solvents at 298-313K,.*Indian Journal of Chem, 37A,* ***1998****, 252-256.*

[4] Ishwara Bhat J.,Sabitha N.V., Acoustic Characteristics of sodium salt of N-Chloro- p- Toluene Sulphamide in aqueous and binary aqueous media at 303k, Indian Journal of Chemistry., 42A **2002**, 520-525.

[5] Koda S.,Matsumota K, Nishimura R.,Ion Association and solvation of Thiocyanates in Water dimethylformamide Mixtures: *An Ultrasonic Study Chem.Soc.Faraday Trans., 87,* ***1991****, 287-291*

[6] K.Takaizumi, *Journal of Solution Chemistry.,29 377(2000)*

[7] A.Karim, S.Labban and Ymarcus, *Journal of Solution Chemistry,Vol 26, 1997 pp 1-12*

[8] M.Nir, I.O Shapiro, R.E Hoffman and M.Rabinovitz, *Journal of Chemical society Perkin Transactions, Vol 8, 1996, pp 1607-1615*

[9] J.I.bhat and Shivakumar H.R, *Journal of.Electrochem.Soc.India, 48,371 (1999)*

[10] *S.Petrucci. Ionic interactions Chapman and Hall, London, 1975*

[11] A .Bhattacharya,J.Dutta,K.Das and K.K.Kundu, Ion- Solvent interactions in some aqueous ethers, *Indian journal of Chemistry, Vol 21A,1982, pp 9-16.*

[12] Nikkam P.S., neena Nikam, Mehdi Hasan ,Suryawanshi B.S., Aoustical properties of Monochloric acid - acetone-water system at different Temperatures, *Asian Journal of.Chem., 6(2), **1994**, 237-24*

[13] Shivakumar H.R., Siju N.Antony., Thermo-acoustical Investigations on Potassium Thocyanate in 2-propanol+ water mixtures, *International Journal of Pure & applied Chemistry, Vol.6no.1Jan-March **2011**, pp. 65-73*

[14] C.J Wilsom and H. H.Wenzkey, J.Chem.Phys.2 (1934)546

[15] K.Srinivasan Manja, Ultrasonic Studies on the nature of molecular interaction in some aqueous, non aqueous solutions and liquid crystals, *university of Madras ,1985.*

[16] S.Thorumaran and D.M.Gardilya. Volumetric and ultrasonic studies on interionic interactions of some amino acids in aqueous magnesium acetate medium at306.15K, *Recent Research in Science and Technology, V o l 3, 2011, pp 56-63*

[17] A.Karim,s.Labban and y.marcus.The solubility and salvation of salts in mixed non aqueous solvents 2: Potassium halides in mixed protic solvents ,*Journal of solution Chemistry,Vol 26,1977 pp 1-12*

[18] S.Chauhan, K. Kumar and B.S Patil, Study of acoustic parameters of proline in lecithin – ethanol at varying temperature, *Indian Journal of Pure and Applied Physics, Vol 51, 2013,pp 531-541*

[19] P.R.Malasane and A.S.Aswar, Thermodynamic and ultrasonic studies of biomolecules in aqueous solutions of metal ion at 303.15 K, *Indian Journal of Chemical Technology, Vol12,2005,pp 689 – 694*

[20] P.S.Nikam and M.Hassan,Ultrasonic velocity and apparent molar compressibility of Trichloroacetic acid in aqueous ethanol, *Asian Journal of Chemistry, Vol5, 1993, pp 319-321*

AN EFFICIENT ALGORITHM FOR THE REMOVAL OF IMPULSE NOISE IN IMAGES USING BLACKFIN PROCESSOR

S. Preethi[1], Ms. K. Subhashini[2]

[1]M.E/Embedded System Technologies, [2]Assistant professor

Sri Sai Ram Engineering College, Chennai (India)

ABSTRACT

In an image transmission process, there are a lot of noises which are usually divided into three groups: Gaussian noise, balanced noise and impulse noise. Impulse noise displays as random white or black dots on an image. It corrupts the image and seriously affects the visual effects. Therefore, the impulse noise reduction has important significance to image processing. For the images corrupted by impulse noise an imperative requirement is to remove the noise impulses without disturbing the edges. The linear filtering techniques are not a proper choice in removing impulse noise. Instead non-linear signal processing techniques such as median filtering should be involved. Median filters have the capability to remove impulse noise as well as preserve the edges. At high noise densities it exhibits blurring and insufficient noise suppression. The median filters operate uniformly across the image and therefore they modify both noise and noise free pixels. Applying median filter unconditionally across the entire image would inevitably alter the intensities and remove the signal details of uncorrupted pixels. To overcome all these drawbacks of median filter an efficient removal impulse noise algorithm is presented for restoration of images that are highly corrupted. This algorithm has much better image quality than a median filter. It removes only corrupted pixel by the median value or by its neighboring pixel value.

Keywords: Impulse noise, Median filter, Dual core. Image restoration, Impulse detection, FEINR

I INTRODUCTION

The images corrupted by impulse noise are often occurred in practice. This type of noise may occur in digital images because of channel decoder damages, dyeing down of signals in communication links, communication subscriber's moving, video sensors noise and other. The impulse noise called salt and pepper causes white and black points appear in digital and gray scale images, which chaotically scattered along image area. Applying of classic median filter for removal of such type of noise gives relatively good results, which are shown in restoring of brightness drops, objects edges and local peaks in noise corrupted images. But analysis of different sources dedicated to median filtering shows that the classic median filter has a set of disadvantages

- signal weakening (object's counters and edges are blurred in image);
- affecting to non-corrupted ("good") image pixels.

For the images corrupted by impulse noise an imperative requirement is to remove the noise impulses without disturbing the edges. Image processing filters require two major characteristics: sufficient noise reduction and

preserving the image edges. Ideally, the filtering should be applied only to corrupted pixels while leaving uncorrupted pixels. Applying median filter unconditionally across the entire image would inevitably alter the intensities and remove the signal details of uncorrupted pixels.

A noise-detection process to discriminate between uncorrupted pixels and the corrupted pixels prior to applying nonlinear filtering is required. Some algorithms for this issue (adaptive median filter, decision based or switching median filters) have been proposed. Possible noisy pixels are identified and replaced by using median value or its variant while leaving uncorrupted pixels unchanged.

These median filters are good at lower noise density levels. The number of replacements of corrupted pixel increases in case of higher noise density. On the other hand, defining a robust decision measure is difficult, because the decision is usually based on a predefined threshold value. If the noisy pixels are replaced by some median value in their vicinity without taking into account the possible presence of edges they are not recovered satisfactorily.

All these drawbacks can be overcome by involving two phases: At first an adaptive median filter is applied for classifying corrupted and uncorrupted pixels; In the second phase a specialized method is applied to the noisy pixels to preserve the edges and noise suppression. But for these algorithms the processing time is very high.

These entire drawbacks can be rectified by the proposed method. The corrupted pixels are replaced by either the median pixel or neighborhood pixel in contrast to other existing algorithms that use only median values for replacement of corrupted pixels. During higher noise densities, the median value may also be a noisy pixel in which case neighborhood pixels are used for replacement; this provides higher correlation between the corrupted pixel and neighborhood pixel. Higher correlation gives rise to better edge preservation. In addition, this algorithm named fast and efficient impulse noise removal (FEINR) uses simple fixed length window of size 3 x 3, and hence, it requires significantly lower processing time compared with other algorithms.

II SYSTEM DESIGN

2.1 System Overview

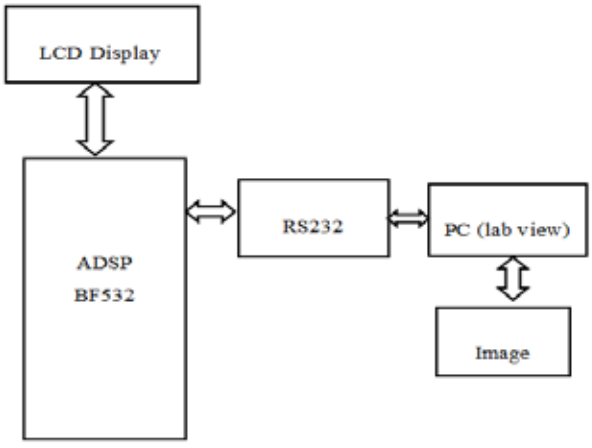

Fig 1.Hardware setup for Impulse Noise Removal

Fig 1 shows the hardware setup for impulse noise removal which is comprised of ADSP BF532 processor, LCD Display, RS232, and a PC for image display. The noisy image is first converted into string using the Labview

software before applying it to the processor. Then the converted string is given to the ADSP processor which is loaded with the noise removal algorithm. Here the noise in the image gets removed and it is sent back to the Labview where the string is again converted into image and it is viewed on the display screen.

2.2 Noise Removal Algorithm

In case of median filtering each pixel isreplaced by the median of its neighborhood values in the current analysis window. The FEINR first detect the impulse noise and then replaces the corrupted pixel. The detection of noisy pixels is decided by checking whether the value of a current pixel lies between the maximum and minimum values that occur inside the selected window. The impulse noise pixels can take the maximum value 255 and minimum values 0. If the value of the pixel processed is within the range, then it is an uncorrupted pixel and left unchanged. If the value does not lie within this range, then it is a noisy pixel and is replaced by the median value of the window. If the noise density is high, there is a possibility that the median value is also a noise value. In the latter case, the pixel processed is replaced by the previously processed adjacent neighborhood pixel value in place of the median value. The FEINR is described below:

1) A two dimensional window, W, of size N x N is selected. We note the pixel to be processed as W(x, y). The parameter N was chosen to be 3.

2) The pixel values inside the window are sorted as follows:

2.1. The minimum value of the elements in the W(x, y) - noted by MIN - is computed.

2.2. The maximum value of the elements in the W(x, y) - noted by MAX - is computed.

2.3. The media value of the elements in the W(x, y) - noted by MED - is computed.

3) In this step the noisy pixel are detected as follows:

- if ((MIN < W(x, y) < MAX) and (MIN>0) and (MAX<255)) then the current pixel W (x, y) is a noise free pixel and it is left unchanged else

- if ((MIN <MED< MAX and (0< MED<255)) then the current pixel is a noisy pixel and it will be replaced by MED.

- if (MED= 0) or (MED=255)) then the median value of the current window is a noisy pixel and the current pixel will be replaced by W(x-1, y) (the left neighborhood of current pixel in the window).

4) Steps 1 to 3 are repeated for the entire image.

In step 4 a new window is acquired by moving toward right the previous window. In fact at each step the processed pixel is the central pixel in the window. The value of the pixel is verified to lies in the range of minimum and maximum values in the windows (previous computed) and that it is true the pixel is decided to be uncorrupted and therefore it is not change. The minimum and the maximum values must not be 0 or 255 values. If the previous condition is not fulfilled the pixel is noisy ant it will be replaced with the median value only if that median value is not itself a noisy value (that is 0 or 255). If so then the corrupted pixel will be replaced with its left neighborhood.

2.3 ADSP Processor Implementation

The ADSP-BF532 processor is a high performance member of the Blackfin family of products targeting a variety of multimedia, industrial, and telecommunications applications. These Blackfin processors combine a dual-MAC state of the art signal processing engine, the advantage of a clean, orthogonal RISC-like microprocessor instruction set, and single instruction, multiple data (SIMD) multimedia capabilities in a single instruction set architecture. The ADSP-BF532 processor has 328K bytes of on-chip memory.

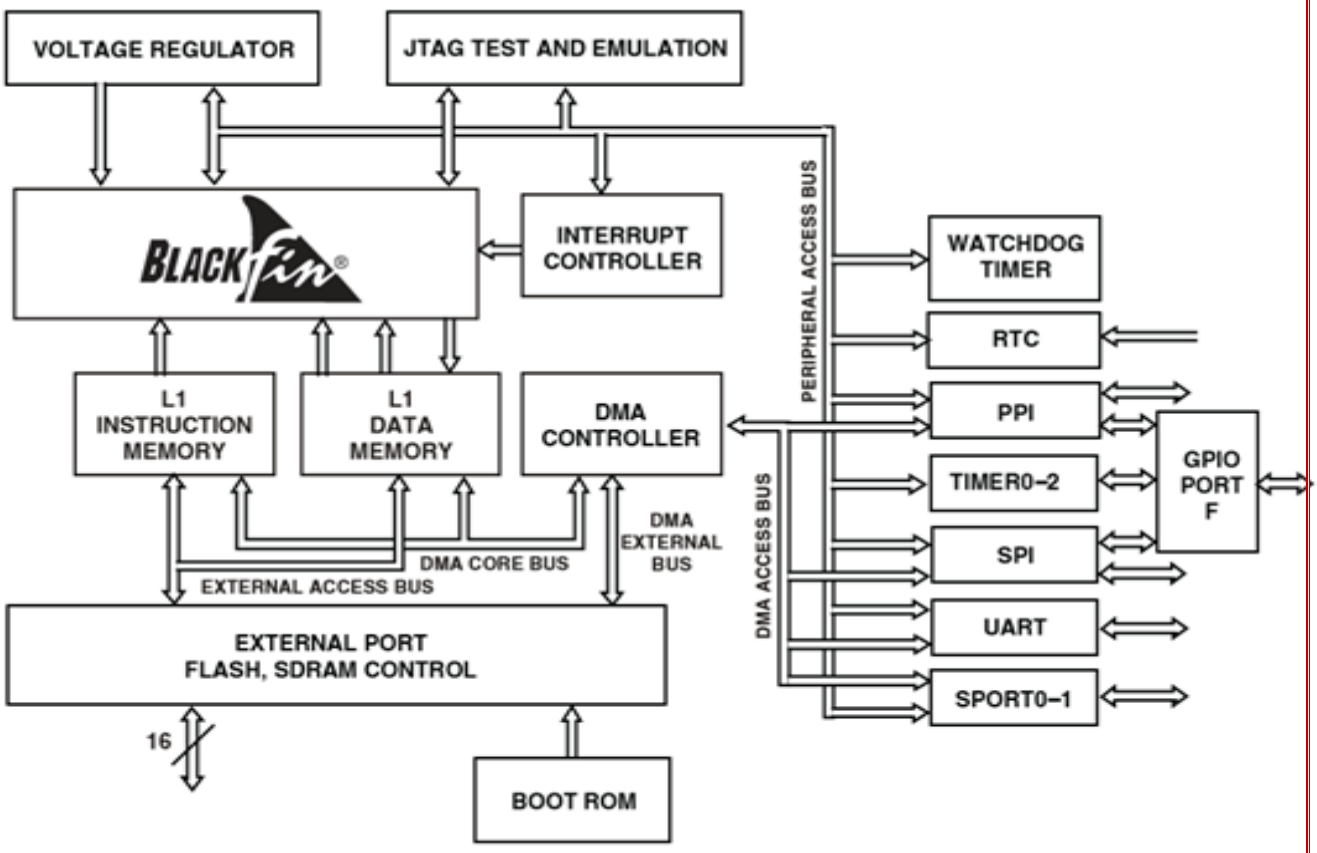

Fig2. Functional Block Diagram

Each Blackfin core includes: • 16K bytes of instruction SRAM/cache • 16K bytes of instruction SRAM • 32K bytes of data SRAM/cache • 32K bytes of data SRAM • 4K bytes of scratchpad SRAM Additional on-chip memory peripherals include: • 128K bytes of low latency on-chip L2 SRAM • Four-channel internal memory DMA controller • External memory controller with glue less support for SDRAM, mobile SDRAM, SRAM, and flash.

The Blackfin processor family includes dual-core processors. In addition to other features, dual-core processors add a new dimension to application development. Each dual-core Blackfin processor has two Blackfin cores, A and B, each with its own internal L1 memory. There is a common internal memory shared between the two cores, and both cores share access to external memory.

Each core functions independently: they have their own reset address, Event Vector Table, instruction and data caches, and so on. On reset, core A starts running from its reset address, while core B is disabled. Core B starts

running when it is enabled by core A. When core B starts running, it starts running its own application, from its own reset address. Having one application per core the full potential of the dual core Blackfin processor is exploiting. Effectively, two single-core applications are building independently, and run in parallel on the processor. The shared memory areas, both internal and external, are each sub-divided into three areas–a section dedicated to core A, a section dedicated to core B, and a shared section. It is left up to the developer to arrange for shared, serialized access to the shared areas from each of the cores.

The Blackfin processor instruction set is optimized so that 16-bit opcodes represent the most frequently used instructions. Complex DSP instructions are encoded into 32-bit opcodes as multifunction instructions. Blackfin products support a limited multi issue capability, where a 32-bit instruction can be issued in parallel with two 16-bit instructions. This allows the programmer to use many of the core resources in a single instruction cycle.

The Blackfin architecture supports instructions that control vector operations. We take advantage of these instructions to perform simultaneous operations on multiple 16-bit values, including add, subtract, multiply, shift, negate, pack, and search.

The vector search instruction is used in a loop to locate a maximum or minimum element in an array of 16-bit packed data. A condition code GE (greater or equal) or LE (less or equal) will be set in the instruction in order to compute the maximum or the minimum value of the vector. Two values are tested at a time. The vector search instruction compares two 16-bit, signed half-words to values stored in the registers of the Blackfin microcontroller. Then, it conditionally updates each register with minimum or maximum of these values. Also, destination pointers are updated based on the comparison, to indicate the position of minimum and maximum in the vector. The above mention instruction may be used in order to find the MIN, MAX and MED values in a given vector W.

The algorithm is the following:

1) Given the vector W of length N = 2M+1 we find the first two maximum values using the vector search instruction with condition code GE.

2) Compare the two maximum values and set the greater of them as MAX value.

3) Discard the two maximum values computed in step 1) and find two minimum values in the remaining vector of length N-2, using vector search instruction with condition code LE.

4) Compare the two maximum values and set the smaller of them as MIN value.

5) Discard the two minimum values computed previously and find two minimum values in the remaining vector, using vector search instruction with condition code LE.

6) Repeat step 5) until the remaining vector has a single component. This component is MED value.

The above algorithm, based on the Blackfin vector search instruction is very computationally efficient.

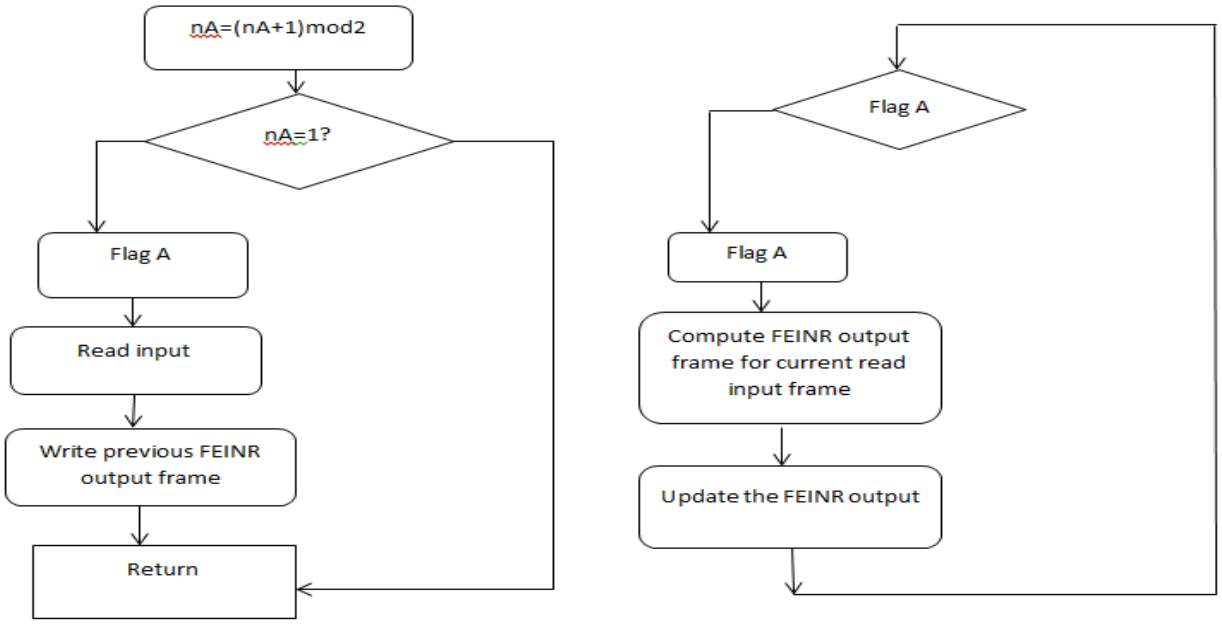

Fig 3.a. Flowchart for core A

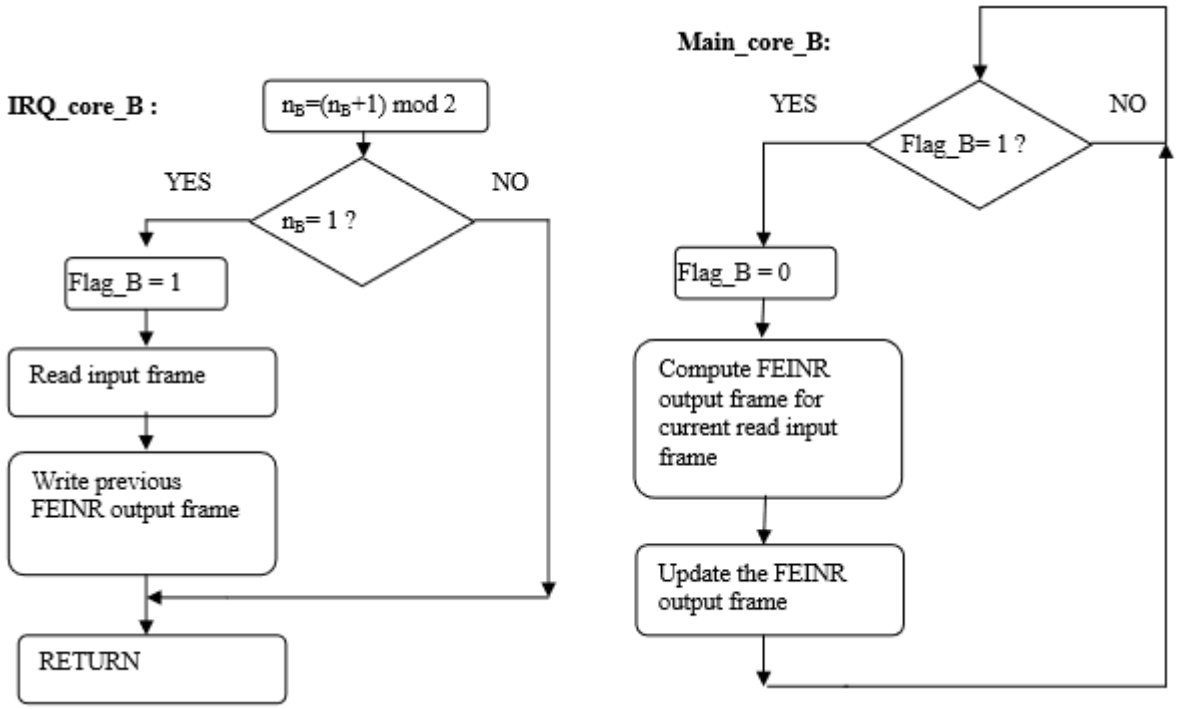

Fig 3.b.Flowchart for core B

In the figure 3.a,b, T_FEINR is the computation time for FEINR algorithm and T represents the frame acquiring interval. Each core in the Blackfin processor has its own interrupts system. We consider that the input frames are acquired from a serial port (SPORT0) that generates a common interrupt for both cores. Each core implements the FEINR algorithm in its own main program (denoted as Main_core_A and Main_core_B) if an appropriate flag (flag_A or flag_B) is set to 1. These flags are set in the interrupt service routines for core A or core B. The main

programs process the odd or the even input frames only. A necessarily functioning condition is that T_FEINR <2T. The computational effort has been estimated. Also, the median filter length will be chosen as 3 x 3 or 5 x 5. These experiments try to estimate how large a processed image may be if we consider that the image processing system has as input video streams at 30 frames per second. The figures 16 and 17 illustrate the computational effort versus image length (we consider an N pixels x N pixels image, where N represents the parameter in the abscise of the graphs in these figures).

2.4 Image Comparison

30% Noise added image

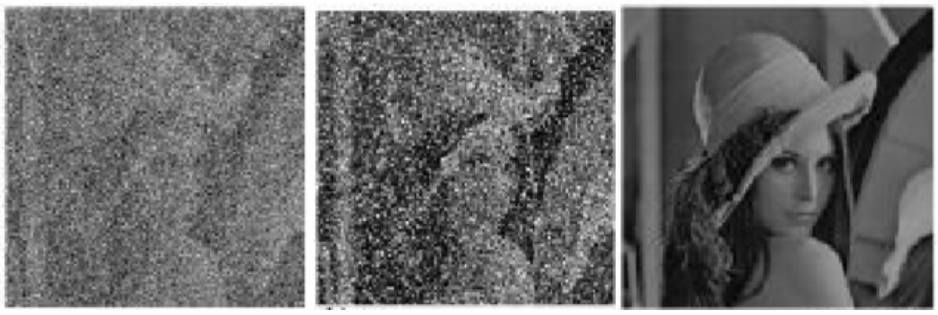

70% Noise added image

III CONCLUSION

An efficient filtering algorithm for impulsive noise removal is presented. This algorithm has significant better performance in terms of noise removal and edge preservation. A fast sorting method, based on vector search instruction of Blackfin microcomputer, is also illustrated. The overall computation time is significantly reduced if such sorting method is used and if a switched buffer technique is involved based on dual core architecture of the Blackfin microcomputer.

REFERENCES

[1] I. Pitas and A. N. Venetsanopoulos, Nonlinear Digital Filters Principles and Applications. Norwell, MA: Kluwer, 1990.

[2] T. Sun and Y. Neuvo, “Detail-preserving median based filters in image processing,” Pattern Recognit. Lett., vol. 15, pp. 341–347, 1994.

[3] S. Zhang and M. A. Karim, "A new impulse detector for switching median filters," IEEE Signal Process. Lett., vol. 9, no. 11, pp. 360–363, Nov. 2002.

[4] ADSP-BF53x/BF56x Blackfin Processor Programming Reference, 2007

[5] Z. Wang and D. Zhang, "Progressive switching median filter for the removal of impulse noise from highly corrupted images," IEEE Trans. Circuits System II, Analog Digit. Signal Processing, vol. 46, no. 1, pp. 78–80, Jan. 1999.

[6] Eduardo Abreu, "A new efficient approach for the removal of impulse noise from highly corrupted images," IEEE Transactions on Image Processing.Vol. 5, No.6, June 1996.

[7]TZU-CHAOLIN AND PAO-TA Yu," Salt-Pepper impulse noise detection and removal using multiple thresholds for image restoration," Journal of Information Science and Engineering 22,189-198 (2006).

[8] Zhou Wang and David Zhang," Progressive Switching Median Filter for the Removal of Impulse Noise from Highly Corrupted Images," IEEE TRANSACTIONS ON CIRCUITS AND SYSTEMS—II: ANALOG AND DIGITAL SIGNAL PROCESSING, VOL. 46, NO. 1, JANUARY 1999.

TEXT-INDEPENDENT SPEAKER RECOGNITION USING SUPERVECTORS

Khurrath-Ul-Aien M.R[1], Anitha G[2]

[1] Scholar, [2]Assistant Professor, Department of computer science and Engineering,

UBDTCE, Davangere (India)

ABSTRACT

In this gives an overview of automatic speaker recognition technology, with an emphasis on text-independent recognition. Speaker recognition has been studied actively for several decades. We give an overview of both the classical and the state-of-the-art methods. We start with the fundamentals of automatic speaker recognition, concerning feature extraction and speaker modeling. We elaborate advanced computational techniques to address robustness and session variability. The recent progress from vectors towards supervectors opens up a new area of exploration and represents a technology trend.

Keywords: Discriminative models , Feature extraction , Text-independence ,Speaker recognition, Statistical models, Supervectors.

I. INTRODUCTION

Speaker recognition refers to recognizing persons from their voice. No two individuals sound identical because their vocal tract shapes, larynx sizes, and other parts of their voice production organs are different. In addition to these physical differences, each speaker has his or her characteristic manner of speaking, including the use of a particular accent, rhythm, intonation style, pronunciation pattern, choice of vocabulary and so on. State-of-the-art speaker recognition systems use a number of these features in parallel, attempting to cover these different aspects and employing them in a complementary way to achieve more accurate recognition. In addition to telephony speech data, there is a continually increasing supply of other spoken documents such as TV broadcasts, teleconference meetings, and video clips from vacations. Extracting metadata like topic of discussion or participant names and genders from these documents would enable automated information searching and indexing. Speaker diarization also known as ‘‘who spoke when”, attempts to extract speaking turns of the different participants from a spoken document, and is an extension of the ‘‘classical” speaker recognition techniques applied to recordings with multiple speakers. In forensics and speaker diarization, the speakers can be considered non-cooperative as they do not specifically wish to be recognized. On the other hand, in telephone-based services and access control, the users are considered cooperative. Speaker recognition systems, on the other hand, can be divided into text-dependent and text-independent ones. In text-dependent systems suited for cooperative users, the recognition phrases are fixed, or known beforehand. For instance, the user can be prompted to read a randomly selected sequence of numbers as described in. In text-independent systems, there are no constraints on the words which the speakers are allowed to use. Thus, the reference (what are spoken in training) and the test (what are uttered in actual use) utterances may have completely different content, and the recognition system must take this phonetic mismatch into account. Text-independent

recognition is the much more challenging of the two tasks. In general, phonetic variability represents one adverse factor to accuracy in text-independent speaker recognition. Changes in the acoustic environment and technical factors (transducer, channel), as well as ‘‘within-speaker” variation of the speaker him/herself (state of health, mood, aging) represent other undesirable factors. In general, any variation between two recordings of the same speaker is known as session variability.

II. DESIGN

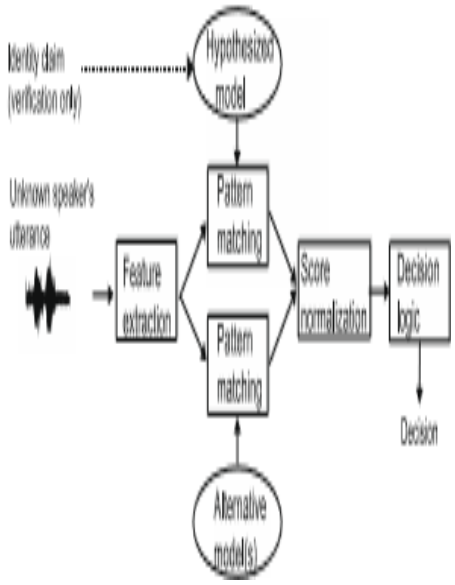

Fig 1: Speaker verification/identification

The feature extraction module first transforms the raw signal into feature vectors in which speaker-specific properties are emphasized and statistical redundancies suppressed. In the recognition mode, the feature vectors extracted from the unknown person’s utterance are compared against the model(s) in the system database to give a similarity score. The decision module uses this similarity score to make the final decision. Virtually all state-of-the-art speaker recognition systems use a set of background speakers or cohort speakers in one form or another to enhance the robustness and computational efficiency of the recognizer.

III. FEATURE EXTRACTION

The speech signal continuously changes due to articulatory movements, and therefore, the signal must be broken down in short frames of about 20–30 ms in duration. Within this interval, the signal is assumed to remain stationary and a spectral feature vector is extracted from each frame. Usually the frame is pre-emphasized and multiplied by a smooth window function prior to further steps. Pre-emphasis boosts the higher frequencies whose intensity would be otherwise very low due to downward sloping spectrum caused by glottal voice source. The window function (usually Hamming), on the other hand, is needed because of the finite-length effects of the discrete Fourier transform. In practice, choice of the window function is not critical. The well-known fast Fourier transform (FFT), a fast implementation of DFT, decomposes a signal into its frequency components. Alternatives to FFT-based signal decomposition such as non-harmonic bases, aperiodic functions. The DFT,

however, remains to be used in practice due to its simplicity and efficiency. Usually only the magnitude spectrum is retained, based on the belief that phase has little perceptual importance. However, provides opposing evidence while described a technique which utilizes phase information. The global shape of the DFT magnitude spectrum known as spectral envelope contains information about the resonance properties of the vocal tract and has been found out to be the most informative part of the spectrum in speaker recognition. A simple model of spectral envelope uses a set of bandpass filters to do energy integration over neighboring frequency bands. Motivated by psycho-acoustic studies, the lower frequency range is usually represented with higher resolution by allocating more filters with narrow bandwidths.

I V. EXPERIMENTAL WORK

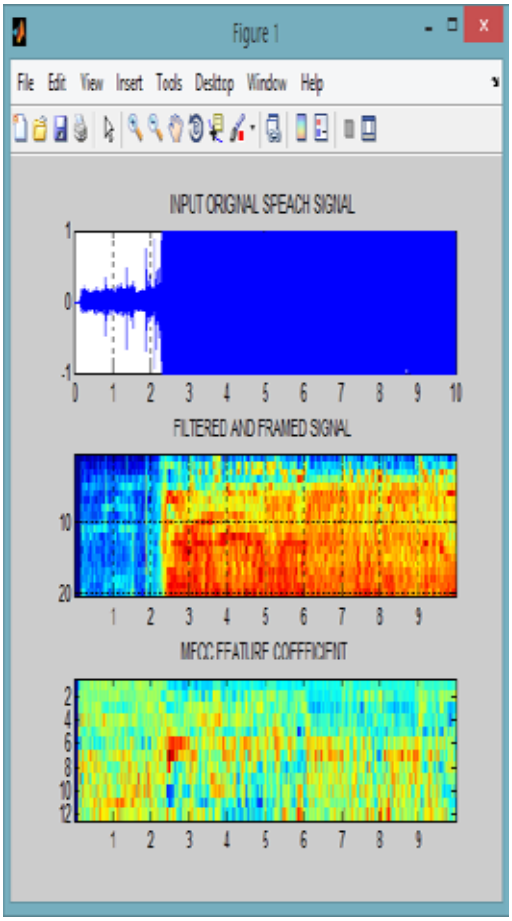

Fig 2: Feature Extracted from Speech

V. CONCLUSION

We have presented an overview of the classical and new methods of automatic text-independent speaker recognition. The recognition accuracy of current speaker recognition systems under controlled conditions is high. However, in practical situations many negative factors are encountered including mismatched handsets for training and testing, limited training data, unbalanced text, background noise and non-cooperative users.

However, many research problems remain to be addressed, such as human-related error sources, real-time implementation, and forensic interpretation of speaker recognition scores.

REFERENCES

[1].Alexander, A., Botti, F., Dessimoz, D., Drygajlo, A., 2004. The effect of mismatched recording conditions on human and automatic speaker recognition in forensic applications. Forensic Science International 146S, December 2004, pp. 95–99.

[2].Besacier, L., Bonastre, J.-F., 2000. Sub band architecture for automatic speaker recognition. Signal Process. 80, 1245–1259. Besacier, L., Bonastre, J., Fredouille, C., 2000. Localization and selection of speaker-specific information with statistical modeling. Speech Comm. 31, 89–106.

[3].Bimbot, F., Magrin-Chagnolleau, I., Mathan, L., 1995. Second-order statistical measures for text-independent speaker identification. Speech Comm. 17, 177–192.

Biographical Notes

Miss. Khurrath Ul Aien M.R is presently pursuing M. Tech. final year in Computer Science and Engineering Department (Computer Science) from UBDTCE, Davangere, India.

Mrs. Anitha G.is working as a Assistant Professor in Computer Science and Engineering Department, from UBDTCE, Davangere, India.

MOLECULAR MODELING STUDY OF VARIOUS SYNTHETIC JHAS CONTAINING VARIED FUNCTIONALITY

Priyanka Sharma[1] and Pamita Awasthi[2]

[1] *Department of Chemistry, Carrier Point University, Hamirpur H.P., (India)*

[2] *Department of Chemistry, National Institute of Technology, Hamirpur H.P. (India)*

ABSTRACT

Virtual screening emerged as an important tool in our quest to access novel pesticides like compounds. The capability to propose feasible ways of binding a putative ligand to a known receptor site is crucial to the structure – based drug design. Molecular docking is one of the most important methods in computer assisted screening of compounds. A docking approach is to "dock" ligand and receptor molecules together in many different ways and then score each orientation by applying different evaluation function. AutoDock 4.2 is an unbiased type docking program in which a ligand finds an optimal position inside the binding cavity of the receptor. In this paper, we reported the protein-ligand interactions using a standard protocol of docking. We have carried out the docking study of a number of synthesized Juvenile Hormone Analogues with receptor binding proteins in order to design targeted JHAs with improved biological activities by understanding their interaction behavior. Among the synthesized derivatives of sulfonamide; 10^{th} analog showed the comparable behavior in terms of their Binding Energy (B.E.) and Inhibitory constant (Ki) with natural JH III and commercial in use IGRs like Pyriproxyfen and Fenoxycarb.

Keywords: ***AutoDock 4.2 software, Juvenile Hormone Analogues, Juvenile hormone binding proteins, Galleria mellonella, Insect Growth Regulators***

I. INTRODUCTION

The study of insect juvenile hormone has assumed great importance because of the possibility of its use as insecticides and pesticides. The use of insect growth regulators such as juvenile hormone and ecdysone has captured worldwide attention in recent past. Insects have a tendency to multiply rapidly; therefore, controlling the vast population of insect is a major problem. The regular and continues use of classical insecticides has made a drastic impact on environment as well as on warm blooded animals. A number of new methods and tools have been proposed in direction of extraction and development of natural and synthetic compounds which should be capable of interfering with growth, development and metamorphosis processes of diverse insect species [1]. These compounds have been called as an insect growth regulators (IGR) or third generation insecticides [2]. Juvenile Hormone (JH) is the main hormone able to regulate all aspects of insect life. They are involved in majority of physiological processes in both developing and mature insects [3]. Juvenile hormone (JH) regulates insect development by bounding to a specific glycoprotein, Juvenile Hormone Binding Protein (JHBP), present in the hemolymph which transport the juvenile hormone (JH) from the site of synthesis to target tissues and serve as JH reservoir. High-affinity juvenile hormone (JH) binding proteins are crucial for proper

insect development, acting as transporters, protectors and reservoirs of the highly hydrophobic and chemically labile JH [4-6]. JH has profound influence on the insect life cycle by hindering larva metamorphosis and by regulating embryogenesis, stimulating reproductive maturation, and controlling the metabolism and migratory behavior of adults. The hemolymph juvenile hormone binding proteins (JHBPs) bind 99% of JH in the hemolymph despite their low abundance, it shows high affinity towards JH molecules (Kd below 10^{-6} M) [7-9]. JHBPs have been isolated from several insect species like *Bombyx mori, Heliothis virescens, Manduca sexta* and *Galleria mellonella*. Among the JHBPs, the protein from *Galleria mellonella* is the object of the present study. *Galleria mellonella,* commonly known as greater wax moth, perceived as the worst beehive pest in the world. Devastation of honeycombs results from the nutritional habits of the larvae, which ingest honey, pollen and wax. *Galleria mellonella* JHBP is a glycoprotein of molecular mass 25880 Da having 245 amino acid residues. Juvenile hormone analogues may act at the membrane level by interacting with various proteins present in the hemolymph or at genetic level by associating with transcription of mRNA [10-15]. They may keep the insects in an immature and potentially injurious stage longer than normal and ultimately affect insect population. Therefore, interest has been generated to design new compounds with different structural features and to study their effect on insect hormonal activity. This will prove very useful in evolving an alternative method in order to avoid the use of toxic chemicals. It has been found experimentally that JHBP of *G. mellonella* undergoes a profound conformational change upon JH binding and this finally provides a foundation for JH docking into JHBP. This leads to a rational approach for designing a large number of molecules that might be used to control insect development [16-18].

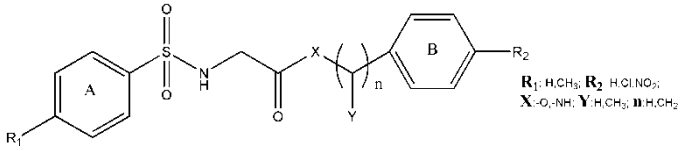

Fig.1 Structure of N-[2-oxo-3-oxa-4-methyl-4- (p-chlorophenyl)butanyl] benzene sulfonamide and analogs (1-10)

In this paper we have reported the docking study of synthesized JHAs containing sulphonamide feature in the main chain with JHBP of *Galleria mellonella*. We have carried out comparative free binding energy analysis of all the synthesized compounds with natural occurring JH III and synthetic IGRs.

II. MATERIAL AND METHOD

2.1 Docking Protocol

The 3D structures of the ligands are constructed using pymol software tool (www.pymol.com) and optimized with AMBER force field of the AutoDock 4.2. The PDB file of the selected structure of *G. mellonella* binding protein (2RCK) is downloaded from the protein data bank. Polar hydrogens are added to the macromolecule (2RCK) using the ADDSOL utility of AutoDock 4.2 (The Scripps Research Institute La Jolla, CA 92037-1000, U.S.A.) and saved in a similar manner as *protein.pdbqt* format. Default values of atomic solvation parameters are used throughout the calculations. Amino acid residues at binding site are selected [9]. Grid box is generated for the calculation of docking interaction energy followed by the generation of grid parameter file *pro.gpf* of protein using AutoGrid Tool of the software. Lamarckian Genetic Algorithm (LGA) protocol is used for protein fixed: ligand flexible model. Lamarckian Genetic Algorithm (LGA) protocol incorporates a local minimization for a given fraction of the population. The LGA mixes a global search for ligand conformation and orientation along with an adaptive local search to perform energy minimization. The scoring function is a sum of Vander

Waals, H-bonding and distance dependent dielectric electrostatics as well as conformational torsional restriction entropy and empirical solvation energetic in terms of ligand-protein complex Docking calculations begins with an initial population of 150 randomly placed conformation of ligands. Therefore, in totality hundred search attempts (ga_run parameter) are performed for each ligand. The maximum number of energy evaluations and generations before the termination of LGA run are 2.5x 10^6 and 2.7 x 10^4 respectively. For the local search, the pseudo-Solis and Wets algorithm are applied. Other docking parameters are set to default values. Final docking orientations lying within 2 Å of the root-mean square deviation (rmsd) tolerance of each other are represented as most favorable conformation with low free energy of binding (ΔG_b). The ligands are ranked according to their binding free energy (B.E.) in kcal/mol and inhibition constant (Ki) in µM at 298.15K. As a results of docking simulation , AutoDock computes intermolecular energy, internal energy and torsional energy as an output; the first two forms the 'docking energy', while the first and the third combine together to give 'binding energy'. [*All the Calculations of Autogrid and Autodock are performed on Linux operating system with system Properties (Intel(R) Pentium(R) D CPU 2.80GHz, 4.0 GB of RAM)]*.

2.2 Virtual screening of JHBP – JHAs complex

We have synthesized Juvenile Hormone mimics with varied functionalities in order to develop better agonist of JH activity in comparison to synthetic IGR like fenoxycarb, S-21149, Compound1 and pyriproxyfen . Docking study of synthesized Juvenile hormone mimics, JH-III and synthetic IGRs with the JHBP of the *Galleria mellonella* is carried out to learn the preferred conformation and configuration of the ligand inside the binding pocket [19-24] (fig 2(a,b)).

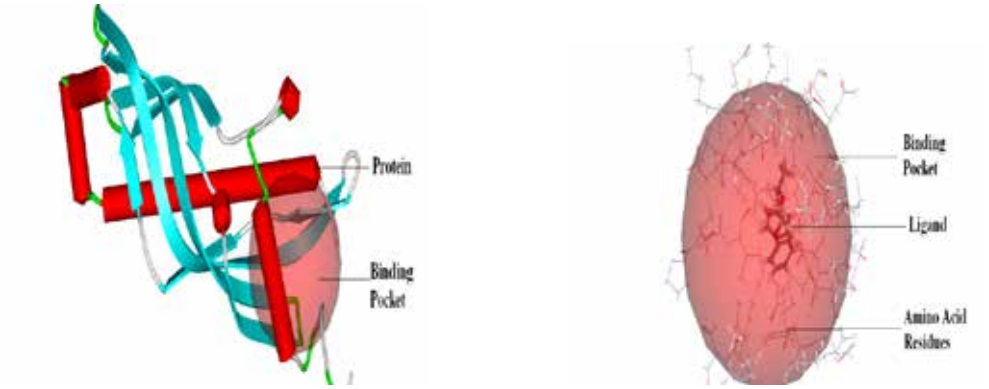

Fig: 2 (A) Complete Structure of The Binding Protein (PDB 2RCK); (B) Ligand Inside Binding Pocket of Protein

Interaction energy of ligands complexed to amino acid residue of binding pocket of the receptor protein is calculated using AUTODOCK 4.2. Docking process in a complex network of interaction is a difficult task. It requires the generation of a large number of configurations of the ligands inside the binding pocket where each being used as an initial docking configuration. Further it identifies the correct pose of the ligand inside the binding pocket and calculates the affinity between the ligand and receptor. The amino acid residues lining inside the pocket region exhibit strong interactions with the synthesized Juvenile Hormone mimics along with JH-III and synthetic IGRs [25-28] . Overall trend for the Binding Energy (BE) Profile is as under:

Pyriproxyfen< Compound 1 < 10 < 4< 8 < 6 < 7 < 9 < 1 <3 < 5 < 2 < S-21149 < Fenoxycarb < Nat. JH III

Among sulfonamide series analog 4, 8 and 10th gave the lowest binding energy profile. All synthetic sulfonamide showed B.E. behavior better then Fenoxycarb, S-21149 and Nat JH III. But higher in comparison to Compound 1 and Pyriproxyfen (Fig. 3).

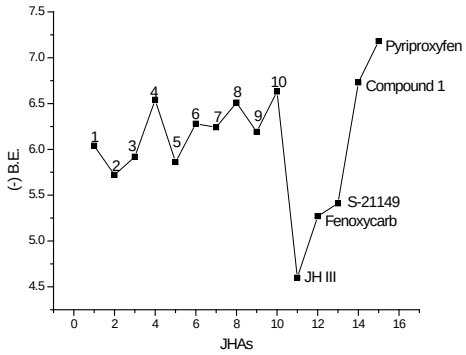

Fig 3: Binding Energy Profile of All The Analogues (1-10) Along With Natural JH III and Synthetic Jhas Fenoxycarb, S-21149, Compound1 and Pyriproxyfen

Protein-ligand binding does not depend only on shape complementary but also on the physiochemical properties. The balance of the Vander Waals, electrostatics, hydrogen bonding and hydrophobic interactions must result in energetically favored binding. Binding is a score of contributing and opposing terms. Therefore, the binding energy is a result of enthalpy-entropy compensation. There are different kinds of interactions operational inside the binding site of the protein depending upon the chemical nature of the ligand molecule. The electrostatic interaction is the main contributor of the interaction energy governing the strength of bonds, the strength of non-bonded interactions and molecular reactivity. In case of the protein-ligand interaction at the active site, ligand experiences a unique environment in terms of electrostatic, steric and hydrophobic properties. Variations in these properties near the active site of the proteins can contribute towards its selectivity and specificity.

In the present study interaction of synthesized JH mimics (1-10), nat JH-III and synthetic IGRs with receptor binding protein at active site show the hydrogen, vander waal and electrostatic interactions. Synthesized JHAs shows main interactions with the binding pocket having amino acid moieties- Thr 22, Tyr 128,130, Lys 218, Ala 21, 220, Ile 18, Cys10 which explain the hydrophobic, acidic and basic nature of the binding pocket. Based upon binding energy profile by docking study we can conclude that sulfonamides along with substituted chloro and phenoxy moiety at the terminal position will be effective IGR In comparison to commercial IGRs. Further replacement of benzene ring by toluene increases the binding energy profile.

III. CONCLUSIONS

In this research paper we have reported the docking study of some of the synthesized JHAs (1-10) having sulphonamide group along with oxa and aza features. In order to design and develop more effective JHAs and to speed up the process ; we have carried out docking study of the synthesized compounds with its receptor site and also compared the study with naturally occurring JH III and commercial in use IGRs (Fenoxycarb, S-21149, Pyriproxyfen and Compound 1). We have studied the receptor –ligand interaction on crystallized JHBP of *G. mellonella*. The crystal structure of JHBPs of *G. mellonella* is established and reported in literature [9]. In order to screen, check and compare the activity of these synthesized JHAs, we have performed docking study using

AutoDock 4.2 software modules and studied receptor-ligand interactions using binding free energy estimation. The docking study of synthesized juvenile hormones and their analogues with the receptor sites in *Galleria mellonella* JHBP suggests that juvenile hormone analogues having minimum score, will fit better inside the binding pocket of the receptor proteins. Aza features corresponds to the more negative score as compared to the oxa feature, therefore, oxa series of compounds believed to be more biological active as compared to aza series. The binding free energy of 10^{th} analog is comparable with natural occurring JH III and Pyriproxyfen. Therefore, 10^{th} analogues containing aza features are suggested to be more effective IGR. In addition to the oxa and aza feature, we have added sulphonamide functionality in the side chain and it has been observed that binding affinity get elevated with the addition of this functionality. We are also in the progress of evaluating this synthetic compound on biological models as well which will be reported later. Besides, further investigation regarding the effect on non-target organism is extremely important and imperative in the near future.

IV. ACKNOWLEDGMENT

Authors thank Sophisticated Analytical Instrument Facility, Punjab University, Chandigarh, for recording FT-IR, NMR (^{1}H and ^{13}C) and mass spectra. We are also thankful to Director, Institute of Biotechnology and Environmental Science- Neri (Hamirpur) H.P for carrying out biological evaluation of the analogs. One of the authors Priyanka Sharma acknowledges MHRD, Government of India for Ph.D. fellowship.

REFERENCES

1. M. Altstein, N. Aharonson & J.J. Menn, Overview: New targets for insect management in crop protection, Arch. Insect Bioche Physiology, 22:5, 1993.
2. L.M. Riddiford, J.W. Truman, Biochemistry of insect hormones and insect growth regulators, Acad Press, New York, 1978, 307.
3. L.M. Riddiford, In: Advances in Insect Physiology. Evans P. D., editor. Vol. 24. London: Academic; 1994, 213–274.
4. H. Tunaz, & N. Uygun, Insect Growth Regulators for Insect Pest Control, Turk. J. Agric. For, 28, 2004, 377-387.
5. W.G. Goodman, N.A. Granger, In: Comprehensive Molecular Insect Science, Elsevier, Oxford, 2005, 319-408.
6. R.P.Braun, G.R.Wyatt, Sequence of the juvenile hormone binding protein from the hemolymph of Locusta migratoria, J. Biol. Chem., 271, 1996, 31756–31762.
7. Q.L. Feng, T.R. Ladd, B.L. Tomkins, M. Sundaram, S.S. Sohi, A. Retnakaran, K.G. Davey, S.R. Palli, Spruce budworm (Choristoneura fumiferana) juvenile hormone esterase: hormonal regulation, developmental expression and cDNA cloning, Mol Cell Endocrinol, 148(1-2), 1999, 95-108.
8. R. Kołodziejczyk, M. Kochman, G.Bujacz, P.Dobryszycki, A. Ożyhar, and M. Jaskolski, Crystallization and preliminary crystallographic studies of juvenile hormone-binding protein from Galleria mellonella haemolymph, Acta Crystallogr., Sect. D: Biol. Crystallogr, 59, 2003, 519–521
9. R. Kolodziejczyk, G. Bujacz, M. Jakób, A. Ożyhar, M. Jaskolski and M. Kochman, Insect Juvenile Hormone Binding Protein Shows Ancestral Fold Present in Human Lipid-Binding Proteins, J. Mol. Biol, 377, 2008,870–881

10. R. Parthasarthy, H. Yu Wu Bai, S.R. Palli, Mechanisms of midgut remodeling: Juvenile hormone analog methoprene blocks midgut metamorphosis by modulating ecdysone action, Mechanism of Development, 123:7, 2006, 530-547.
11. S.R. Palli, K. Touhara, J.P. Charles, B.C. Bonning, J.K. Atkinson, S.C. Trowell, K. Hiruma, W.G. Goodman, T. Kyriakides, G.D. Prestwich, B.D. Hammock and L.M. Riddiford, A nuclear juvenile hormone-binding protein from larvae of Manduca sexta: a putative receptor for the metamorphic action of juvenile hormone, Proc Natl Acad Sci U S A., 91(13), 1994, 6191–6195.
12. J.R. Wisniewski, M. Kochman**,** Juvenile-hormone-binding protein from silk gland of Galleria mellonella, Federation of European Biochemical Societies, 171: 1,1984, 127-130.
13. K.A. Lerro, G.D. Prestwich, Cloning and Sequencing of a cDNA for the Hemolymph Juvenile Hormone Binding Protein of Larval Manduca sexta, Journal of Biological Chemistry, 265(32),1990,19800-19806.
14. L.I. Gilbert, N.A. Granger, R.M. Roe, The JHs: historical facts and speculations on future research directions, Insect Biochem Mol Biol, 30, 2000, 617–644.
15. K. Touhara, G.D. Prestwich, Binding site mapping of a photoaffinity-labeled juvenile hormone binding protein, Biochem Biophys Res Commun., 182 (2), 1992, 466-473.
16. S. Sasorith, I.M.L. Billas, T. Iwema, D. Moras, J.M. Wurtz, Structure-based analysis of the ultraspiracle protein and docking studies of putative ligands, Journal of insect science, 25(2), 2002,11.
17. J. Wang, P.A. Kollman, I.D. Kuntz, Flexible ligand docking: A multistep strategy approach, Protein: Structure, Function, and Genetics, 36,1999, 1-19.
18. A. M. Manikrao, P.N. Khatale, R.D. Jawarkar, J.V. Vyas, D.T. Mahajan, V. H. Masand, T. Hadda, Presuming the Probable Anti-inflammatory Mechanism of Ursolic Acid: a plant derived pentacyclic triterpenoid, using molecular docking, J. Comput. Method. Mol. Design, 1(2), 2011,9-13.
19. G.M. Morris, D.S. Goodsell, R.S. Halliday, R. Huey, W.E. Hart, R.K. Belew and A.J. Olson, Automated Docking Using a Lamarckian Genetic Algorithm and Empirical Binding Free Energy Function, J Comput Chem, 19, 1998, 1639-1662.
20. E. Jenwitheesuk, R. Samudrala, Improved prediction of HIV-I protease-inhibitor binding energies by molecular dynamics simulations, BMC Structural Biology, 3:2, 2003.
21. A.A. Joshi, C.L. Viswanathan, Docking studies and development of novel5-heteroarylamino-2,4-diamino-8-chloropyrimido-[4,5b]quinolines as potential antimalarials, Bioorganic & Medicinal Chemistry Letters,16, 2006, 2613.
22. P.R. Andrews, D.J. Craik, J. L. Martin, Functional Group Contributions to Drug-. Receptor Interactions, J. Med. Chem., 27, 1984, 1648-1657.
23. E.X. Esposito, K. Baran, K. Kelly, J.D. Madura, Docking of Sulfonamides to Carbonic Anhydrase II and IV, Journal of Molecular Graphics and Modelling, 18, 2000,283.
24. J.Y. Trosset, H.A. Scheraga, PRODOCK: a new software package for protein modeling and docking, J. Comput. Chem, 20, 1999, 412.
25. P. Awasthi, and P. Sharma, Computer aided designing of Juvenile Hormone Analogues as a potent pesticide based on Ligand - receptor interaction - A Docking Study, Proceeding of the 2010 International Confrence on Bioinformatics & Computational Biology, CSREA Press, pp 634-639, ISBN:1-60132-132-5.

26. P. Awasthi, and P. Sharma, In silico screening of Juvenile Hormone Analogues: a docking study, International Conference on Advances in Computing and Communication, 2011, pp 652-654, ISBN: 978-81-920874-0-5.
27. P. Awasthi, P. Sharma, In silico screening of the juvenile hormone analogues with juvenile hormone binding protein of Galleria mellonella - a docking study, SAR and QSAR in Environmental Research, 23:7-8, 2012, 607-625.
28. P. Awasthi and P. Sharma, Designing and Binding Mode Prediction of Juvenile Hormone Analogues as Potential Inhibitor for Galleria mellonella, Journal of Computer Science& System Biology, 6:3, 2013.

7

THE SYSTEMATIC DEPENDENCE OF (E2;4G→2G)/B(E2;2G→0G) RATIO ON N AND Z FOR ND-HG NUCLEI

Satendra Sharma[1], Reetu Kaushik[2]

[1]*Department of Physics, Yobe State University, KM 7, Gujba Road, P. M. B. 1144, Damaturu, Yobe State, (Nigeria)*

[2]*Research Scholar, Department of Physics, Mewar University, Gangrar, Rajasthan, (India)*

ABSTRACT

The systematic dependence of experimental B(E2; 4g→2g)/ B(E2;2g→0g) branching ratio with N and Z is carried out for Nd- Hg even –even nuclei. The SU(5) and SU(3) limits of interacting boson model are also discussed. The N and Z dependence of B(E2) branching ratio has been observed. The Z=64 subshell effect is also seen for N≤ 90 region.

Keywords: B(E2; 4g→2g)/ B(E2;2g→0g) branching ratio, nuclear structure, Nd –Hg nuclei, SU(5), SU(3), Z=64 subshell effect

I. INTRODUCTION

The concept of collectivity in nuclei is one of the most fundamental findings in history of nuclear physics. Various nuclear models have been applied to describe this collective behaviour of atomic nuclei. The geometrical models depicting the nucleus as a liquid drop with a given nuclear shape and algebraic models, take into account the pairs of proton and/or neutron only. Despite the often very dissimilar theoretical approaches, most of the collective models have some common basic features, such as predictions of energies rotational, vibrational and other higher multi-phonon bands or B(E2) ratios for inter and intra band transitions, which have been observed in a wealth of non- magic atomic nuclei.

The energy ratio R_4 is a key observables which can be used to assess the collectivity of nuclei and it is equal to 2 for an ideal spherical harmonic vibrator or SU(5) limit and 10/3 in an axially symmetric deformed rotor or SU(3) limit of interacting boson model (IBM)[1]. The transition rates also provide another good measure of nuclear collectivity [2], which is less sensitive to anharmonicities than energies of various bands. The $B(E2;4_g\rightarrow2_g)/B(E2;2_g\rightarrow0_g)$ branching ratio is a particularly good example, which is equal to 2 in the spherical limit or SU(5) and 1.4 in the deformed limit or SU(3)[1]. Significant deviations from these two limiting values can be found; if one moves away from the closed shell.

In the present work, we have compiled the observed data of $B(E2;4_g\rightarrow2_g)/B(E2;2_g\rightarrow0_g)$ branching ratio from the website of Brookhaven National Laboratory[3] for Nd – Hg nuclei. The variation of this B(E2) ratio with N and Z has been studied. The SU(3) and SU(5) limits are also included for useful comparison. The result & discussions and conclusion are given in § II and III respectively.

II.RESULT AND DISCUSSIONS

2.1 The variation of experimental B(E2;4g→2g)/ B(E2; 2g→0g) ratio verses neutron number (N)

To avoid the overlapping of experimental data of the nuclei and to have a clear picture for a definite conclusion about the dependence of B(E2;4g→2g)/B(E2;2g→0g) ratio on N, the whole data is divided into two parts and shown in two figures i.e. Fig. 1 for Nd- Er nuclei and in Fig. 2 for Yb- Hg nuclei. The vibrational model or SU(5) limit at 2 and rotational model or SU(3) limit at 1.4 are shown in the Fig 1 and Fig. 2. The data points are joined for same value of Z, so that the effect of N will be visible.

For Nd, this ratio increases sharply from 0.73 to 1.61(maximum value at N=88) as N increases from 84 to 88 and if N is further increased from 88 to 92 it decreases slowly from 1.61 to 1.31(see Fig. 1). The same feature is observed for Sm, where this ratio increases from 1.65 to 1.9 on increasing N from 86 to 88 and beyond N=88 it drops sharply and approaches to Alaga value of 1.4 for N=92. In case of Gd, the BE(2) ratio decreases from 1.82 to 1.46 as N increases from 88 to 94. Also in Er, this ratio decreases from 1.78 to 1.5 as N increases from 88 to 100 and minimum value of 1.18 at N=96. Therefore, for N=88 (Sm, Gd and Er) isotones, this ratio ≈1.8 is very close to the VM limit of 2.0 indication vibrational nature. However for Dy (N=88, 92, 94, 96) this ratio is close to Alaga value indication deformed rotor nature and for N=90; Dy indicating transitional nature because this ratio (=1.63) is lying in between SU(5) and SU(3) limiting value (see Fig. 1).

For Yb and Hf nuclei, BE(2) ratio is ranging between 1.4 to 1.6 for different values of N and close to SU(3) limit (see Fig. 2). In case of W, the ratio increases sharply from 1.1(3) to 1.74(15) on increasing N from 94 to 100 and decreases very slowly on increasing N from 108 to 112 (almost remains around Alaga value).

For N=96 the data point of Os is close to the other N=96 isotones (Yb, Hf, W) data points. When N increases from 108 to 112, the ratio for Os increases from 1.4(4) to 1.68(11) and when N is increased from 112 to 116 the B(E2) ratio decreases from 1.68(11) to 1.22(4) indicating prolate to oblate shape-phase-transition as observed by Kumar and Baranger [4].

For N=98, the B(E2) [=1.87(24)] for Pt is close to VM value and for N=102 the ratios is minimum [=0.92(22)]. The B(E2) ratio for Pt decreases from 1.65 to 1.56 when N increases 106 from 114 and again increases from 1.56 to 1.73 as N increases from 114 to 116(attains maximum value =1.73(11) at 116). If N is increased from 116 to 120 this ratio drops linearly with the same slope as observed for Os (N=112 to 116).This indicates the similar nature of Pt and Os nuclei for this region.

For two nuclei; ^{182}Hg and ^{184}Hg; the B(E2) ratio is 4.6(3) and 2.8(8) respectively; which are anomalously more than VM limiting value and not included in the Fig.2. The B(E2) ratio is smallest in case of ^{198}Hg; which is non magic nucleus; has only two vacancy of p+ for Z =82. This ratio is also very small in case of $^{144}Nd_{84}$ [=0.73(9)] (see Fig.1); which is also a non- magic nucleus; which has only two valence n^0 outside N=82. It supports the findings of Cakirli et.al. [5], that the B(E2;4g→2g)/B(E2;2g→0g) ratio is anomalously small in non magic nuclei, as it cannot be explained with collective approaches.

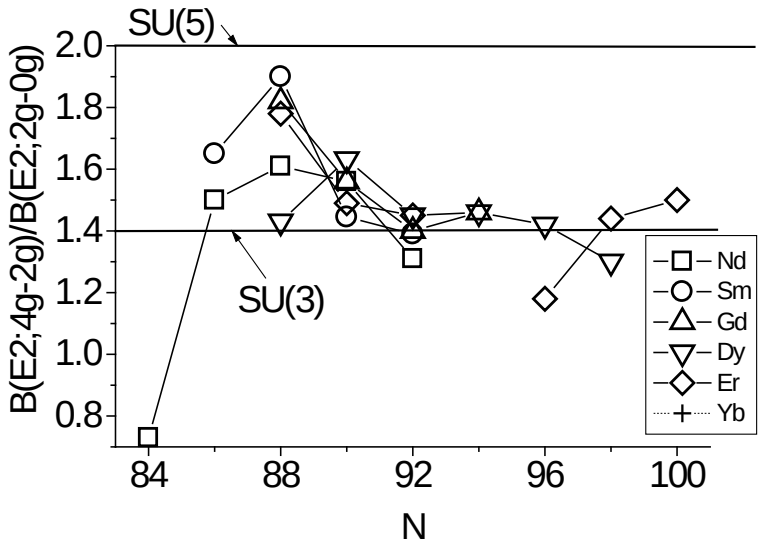

Fig.1: The variation of experimental B(E2;4g→2g)/B(E2;2g→0g) ratio vs. neutron number (N) for Nd-Er nuclei. The vibrational limit SU(5) at 2.0 and rotational limit SU(3) at 1.4 are shown by dotted lines for comparison.

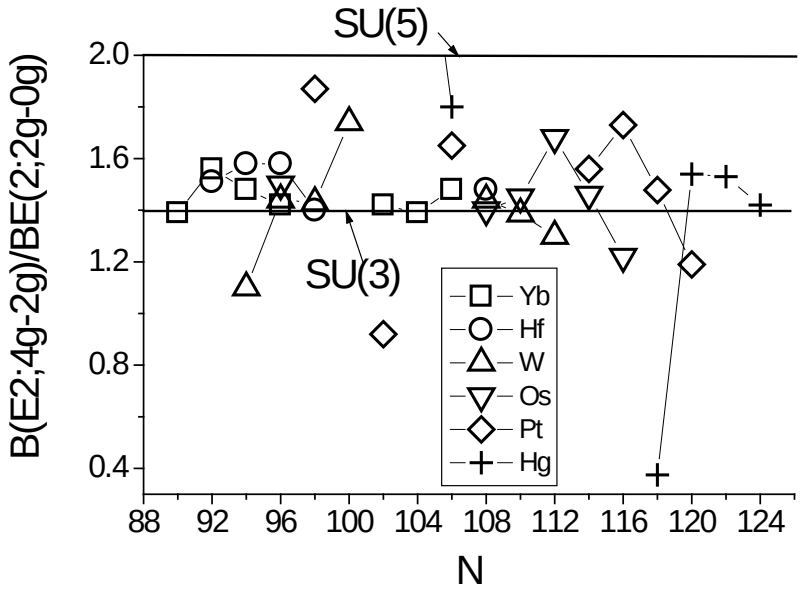

Fig.2: The variation of experimental B(E2;4g→2g)/B(E2;2g→0g) ratio vs. neutron number (N) for Yb-Hg nuclei. The vibrational limit SU(5) at 2.0 and rotational limit SU(3) at 1.4 are shown by dotted lines for comparison.

2.2 The variation of experimental B(E2;4g→2g)/ B(E2; 2g→0g) ratio verses proton number (Z).

The variation of observed B(E2;4g→2g)/ B(E2; 2g→0g) ratio with proton number (Z) is shown in Fig. 3, 4 and 5 for N=84 to 92, N=94 to 102 and N= 104 to 124 isotones respectively and the experimental points are joined for same value of N to observe the effect of Z. The vibrational limit (VM) or SU(5) at 2 and rotational limit or SU(3) at 1.4 are also shown by dotted lines for useful comparison in each figure.

It is evident from Fig. 3, that the BE(2) ratio for N=88 isotones increases on increasing Z from 60 to 62 (attains the maximum values for Sm_{88}) and decreases for Gd and Dy (attains minimum value close to SU(3) limit for Dy_{88}) and again for Er it increases. For N=88, the B(E2) ratio is close to SU(5) limiting value for Sm, Gd and Er while Dy reflects SU(3) nature and Nd in between these two limits. Also, the Sm_{88} is least deformed and Dy_{88} is most deformed. For N=86 isotones the B(E2) data is available only for two nuclei and it is increasing on increasing N from 60 to 60 as in the case of N=88.

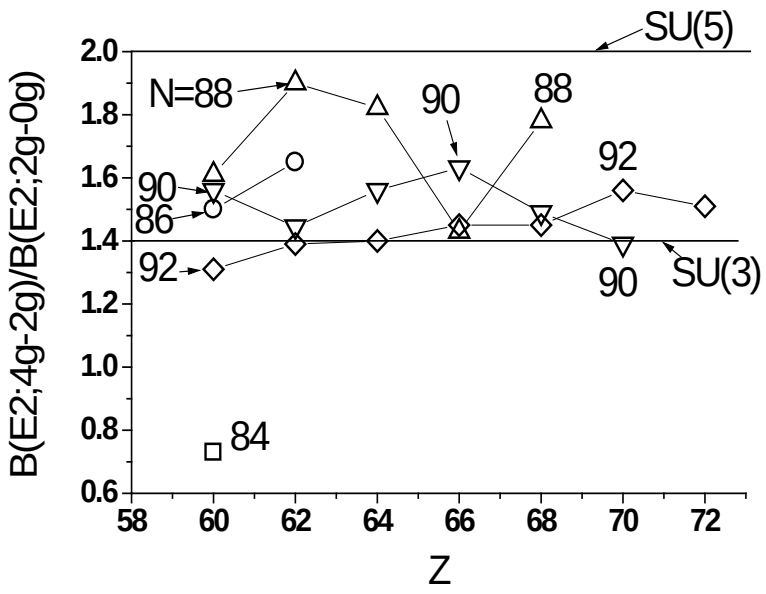

Fig.3: The variation of experimental B(E2;4g→2g)/ B(E2; 2g→0g) ratio vs. proton number (Z). The vibrational limit SU(5) at 2.0 and rotational limit SU(3) at 1.4 are shown by dotted lines for comparison. The experimental points are joined for same value of N to observe the effect of Z on this B(E2) ratio for each isotones for N=84-92.

For N=90 isotones the behaviour of B(E2) is just opposite to N=86 and 88; the B(E2) ratio initially decreases as N increases from 60 to 62 and increases as N increases from 62 to 66 just opposite to N=88. It is evident from the figure that the gap is maximum between the two curves for N=88 and 90 around Z= 64 indication the subshell effect at Z=64 for N<90. It is supporting the findings of Casten [6] and Casten and Zamfir [7].

In general, for N=90 isotones, the B(E2) ratio is somewhat independent of Z indicating constant structures because the values of this ratio are ranging between 1.45 to 1.6 and it support the findings of Gupta [8]. For N=90 isotones, this B(E2) ratio initially decreases on increasing Z from 60 to 62 (attains minimum values which is close to SU(3) limiting value for Sm_{90} unlike Sm_{88} for which this ratio is close to SU(5) limiting value) and

increases slowly on increasing Z from 62 to 66; and attains maximum value(=1.6) for Dy_{90}; and beyond Z=66 the BE(2) decreases linearly on increasing Z from 66 to 70 (and approaches 1.4 value for Hf_{90}). It is clear from Fig. 3 that Sm_{90} and Hf_{90} are most deformed in comparison to other N=90 isotones.

For N=92 isotones, this ratio goes on increasing very slowly from 1.31 to 1.56 on increasing Z from 60 to 74 and is close to SU(3) limiting value of 1.4. However for N=94, this ratio is almost constant because its values are 1.46±0.05, 1.46±0.07, 1.48±0.07, 1.58±0.10 and 1.1±0.3 for Gd, Dy, Yb, Hf and W isotopes respectively indication Z independency. For N=94, 96 and 98 isotones (see Fig. 4) the ratio is close to SU(3)

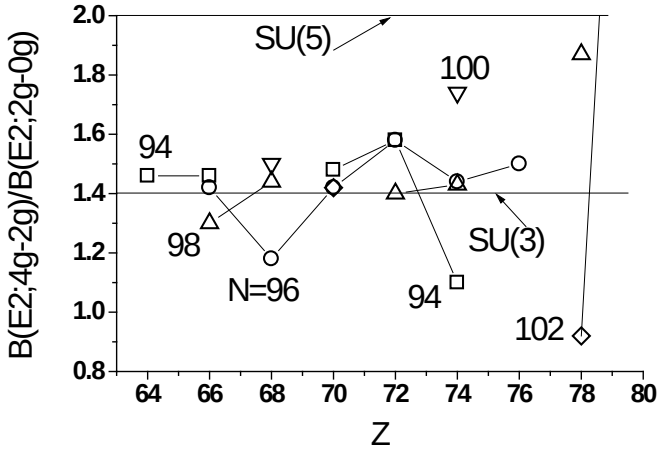

Fig.4: Same as Fig.3 for N=94 to 102.

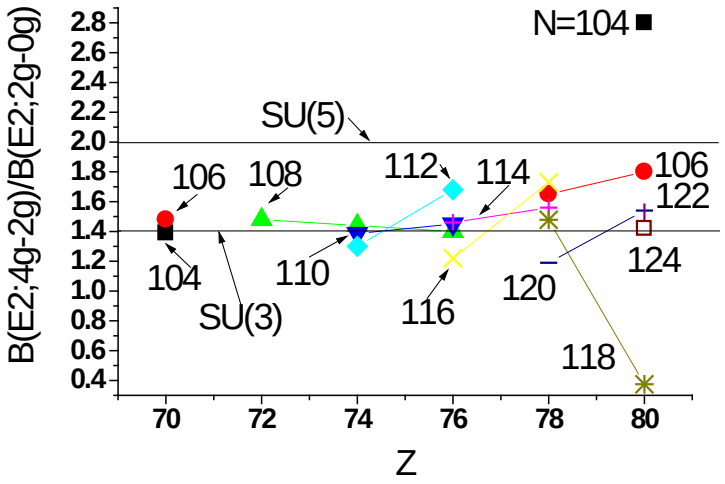

Fig.5: Same as Fig.3 for N=104 to 124.

limiting value indicating deformed nature. For other isotones the B(E2) ratio is lying between SU(5) and SU(3) or O(6) limiting values (see Fig.5) as predicted by the asymmetry rotor model [9].

III. CONCLUSION

The variation of B(E2; 4g→2g)/ B(E2;2g→0g) ratio with N and Z is shown for Nd – Hg nuclei. It is found that the there is shape phase transition for N=88 and 90 isotones (Nd, Sm, Gd, Er) from an ideal spherical harmonic vibrator or SU(5) to an axially symmetric deformed rotor or SU(3). Also B(E2) ratio is anomalously small for two nuclei i.e., $^{198}_{80}Hg_{118}$ (=0.375±0.018) and $^{144}_{60}Nd_{84}$ (=0.73±0.090) with only two vacancy of p+ for Z =82 and two valence n^0 outside N=82, respectively; which supports the findings of Cakirli et.al. [5]. The present study supports; the subshell effect around Z=64, for N≤ 90 as observed by Casten [6] and Casten and Zamfir [7]; and the constant nuclear structure of N=90 isotones as pointed out by Gupta [8].

IV.ACKNOWLEDGEMENTS

One of us (SS) expresses his gratitude to the Prof. Alabi Musa, Vice Chancellor, Yobe State University, Damaturu, Yobe State, Nigeria for encouragement and for providing the facilities for the research work. We are grateful to Professor J. B. Gupta, Ramjas College, University of Delhi for his valuable guidance.

REFERENCES

[1] R. F. Casten, *Nuclear Structure from a Simple Perspective,* Oxford University Press, New York, 1990. F. Iachello and A. Arima, *The Interacting Boson Model,* Cambridge University Press, Cambridge, 1987.

[2] A. Bohr and B. R. Mottelson, *Nuclear Structure, Vol. II, Benjamin, New York, 1975.*

[3] http://www.nndc.bnl.gov

[4] K. Kumar & M. Baranger, **"**Nuclear deformations in the pairing-plus-quadrupole model (V).: Energy levels and electromagnetic moments of the W, Os and Pt nuclei", *Nucl. Phy. A 122 (1968) 273-324.*

[5] R. B. Cakirli, R. F. Casten, J. Jolie, and N. Warr, "Highly anomalous yrast B(E2) values and vibrational collectivity", *Phys. Rev. C 70 (2004) p. 047302.*

[6] R. F. Casten, "NpNn Systematics in Heavy Nuclei", *Nucl. Phys. A443, 1 (1985).*

[7] R. F. Casten and N. V. Zamfir, "The evolution of nuclear structure: the NpNn scheme and related correlations", *J. Phys. G Nucl. Part. Phys.* 22, 1521(1996).

[8] J. B. Gupta, "A microscopic explanation of the isotonic multiplet at N = 90 and of the F-spin multiplet in Dy-Hf", *Eur. Phys. J. A. 48(2012)177.*

[9] Satendra Sharma and Reetu Kaushik, "Test of Asymmetry Rotor Model for the B(E2;4g→2g)/B(E2;2g→0g) Branching Ratio in Medium Mass Region", *International Journal of Computer & Mathematical Sciences, Vol. 4, Special Issue (2015) p. 160-167.*

Biographical Notes

Dr. Satendra Sharma is working as Professor and Head, Department of Physics, Yobe State University, Damaturu, Yobe State, Nigeria.

Mrs. Reetu Kaushik is a research Scholar in the Department of Physics, Mewar University, Gangrar, Rajasthan, India. She has published 01 research papers in International Journal, 6 papers in the Proceedings of Department of Atomic Energy Symposium on Nuclear Physics and 1 paper in International Conference.

DESIGN AND IMPLEMENTATION OF DC MOTOR SPEED CONTROL BY ARMATURE VOLTAGE VARIATION USING WIRELESS TECHNOLOGY

Sreeparna Dasgupta [1] , Reshma Sengupta [2]

[1,2]Asst. Prof., Department of Applied Electronics and Instrumentation Engineering, Heritage Institute of Technology, Kolkata,(India)

ABSTRACT

This paper presents a scheme for the speed control of a dc motor by changing its armature voltage using wireless technology. Here the remote node consists of two RF transceivers, along with signal conditioning circuits. The motor speed is sensed by an encoder, and feedback signal is transmitted wirelessly to the Base Station equipped with another RF transceiver module. The required control action is taken by the Base Station PC and again transmitted wirelessly to the remote node. This work does not need any WSN platform and remote nodes do not require additional processor hardware.

Keywords: Application Programming Interface, API data frame, Encoder, RF transceiver, Xbee, Zigbee

I. INTRODUCTION

A Wireless Sensor Network (WSN) is a collection of a large number of smart sensor nodes, consisting of radio frequency (RF) transceivers, sensors, micro-controllers and power sources – thereby imparting computational and communication capabilities along-with sensing functions to them. Advances in wireless sensor networking technology have led to the development of low cost, low power WSNs which are being increasingly used in diverse application areas not only for sensing and data acquisition but also for controlling end devices [1], [2].

A general WSN protocol consists of the application layer, transport layer, network layer, data link layer, physical layer, power management plane, mobility management plane and the task management plane. Currently two standard technologies are available for WSN : ZigBee and Bluetooth. Both operate within the Industrial Scientific and Medical (ISM) band of 2.4 GHz, which provides license free operations, huge spectrum allocation and worldwide compatibility [3].

In this work wireless technology has been used to control the speed of a dc motor at the desired value by changing the armature voltage. The remote node consists of two RF transceiver devices, digital to analog converter, and some signal conditioning circuits. Here a single remote node has been used for both sensing and actuation but with separate RF transceivers. The control algorithm resides in the Base Station PC. The control output generated there is transmitted in coded form by the RF transceiver to the Remote node. The control signal received at the Remote node is suitably processed to effect change of speed.

II. WIRELESS TECHNOLOGY

Wireless technology is based on RF data transmission and ZigBee is a standard RF communication protocol for low-power, wireless mesh networking and XBee is a brand of radio that supports a variety of communication protocols, including ZigBee, 802.15.4, and WiFi, among others. ZigBee defines three different device types: coordinator, router, and end device having different functions and privileges. Each zigbee network is defined with a unique PAN identifier (PAN ID) which is common among all devices of the same network. ZigBee devices are either preconfigured with a PAN ID to join, or they can discover nearby networks and select a PAN ID to join. XBee modules support 16 operating channels in the 2.4 GHz frequency band.

Data transmission in Zigbee can be either unicast or broadcast. Unicast transmissions are sent from one source device to another destination device. Broadcast transmissions are intended to be propagated throughout the entire network such that all nodes receive the transmission. Xbee module has two communication modes - Transparent mode and API mode. In transparent mode, The data received by the DIN pin is transmitted via antenna, and the data received via antenna is sent out through the DOUT pin [4].

The module configuration parameters are configured using the AT command mode interface. API (Applicatio Programming Interface) extends the level to which a host application can interact with the networking capabilities of the module. API mode transfers data in formatted frame. The data needs to be formatted according to the frame type as per the requirement of the application. There are different types of frame such as ‘ AT Command’ type, Transmit

Request type, ‘Explicit Addressing Frame’ type, ‘Remote AT command’ type and many more. In this work for sending the control signal to the remote device ‘Remote AT command frame ‘ type is used provided the IO sampling rate for the RF modules are properly set. For getting the present value of 16 bit network address of the RF modules ‘Transmit Request frame‘ type is used.

III. DATA TRANSMISSION USING API

API data frame comprises of Start Delimiter, Length, Frame Data and Checksum. API framed data starts with ‘Start Delimiter’ as 0x7E, ‘Length’ indicates the number of bytes of data being sent. It is divided in 2 bytes (MSB & LSB) for the length over 255 bytes. The ‘Frame Data’ is made up of ‘API Identifier’ and ‘cmdData’. The first one specifies the selected frame type and the last one comprises of ‘Frame ID’, ‘Destination Address’, ‘Options’ and ‘RF Data’. The ‘Frame ID’ identifies the UART data frame for the host to match with a subsequent response. If it is zero, no response is requested. There are 64 bit ‘Destination Address’ as well as 16 bit ‘Destination Address’. The first one just represents the serial number of the destination XBee module and the second one indicates the destination network address. Both of these if not known can be represented by FFFE for broadcasting to all devices including sleepy devices. By giving right byte value to the ‘options’ special functions can be allowed. Next is the RF data for transmission. The ‘Checksum’ is calculated by subtracting the sum of the byte values after ‘Length’ upto ‘Checksum’ from FF [5].

IV. SYSTEM DESIGN

The major hardware components include XBee Series2 IC, DAC 0808, LM 317, F/V Converter, I/V Converter, Speed sensor, DC motor (12 V, 0.1 A, 30 rpm), power supplies. The circuit developed is shown in Fig 1.

The Xbee Series 2 IC is a microchip from Ember Networks and requires 3.3V power supply for its working and has a whip antenna for RF transmission. Its indoor range of communication is 30m whereas outdoor range is 90m. In this work three XBee series2 modules have been used, one as a coordinator (base station) and other two as end device one for sensing and and the other for actuation, henceforth referred to as Sensing XBee and Actuation XBee respectively.

The XBee USB Adapter provides a serial interface using the FTDI USB serial interface chip (FT232RL) and virtual COM port drivers to emulate a serial COM port. This interface has been used to send/receive serial data between the PC and the coordinator XBee for communication and configuration.

For configuring the XBee modules as coordinator or end device, XCTU software of Digi International is required. The baud rate (9600) setting for communication, PAN ID verification, channel synchronization, destination address setting for both the coordinator and end device are done through this software. Loop back testing ensures that the two XBee modules communicate with each other properly and at the configured Baud Rate. The control algorithm has been implemented in C++.

Remote Node

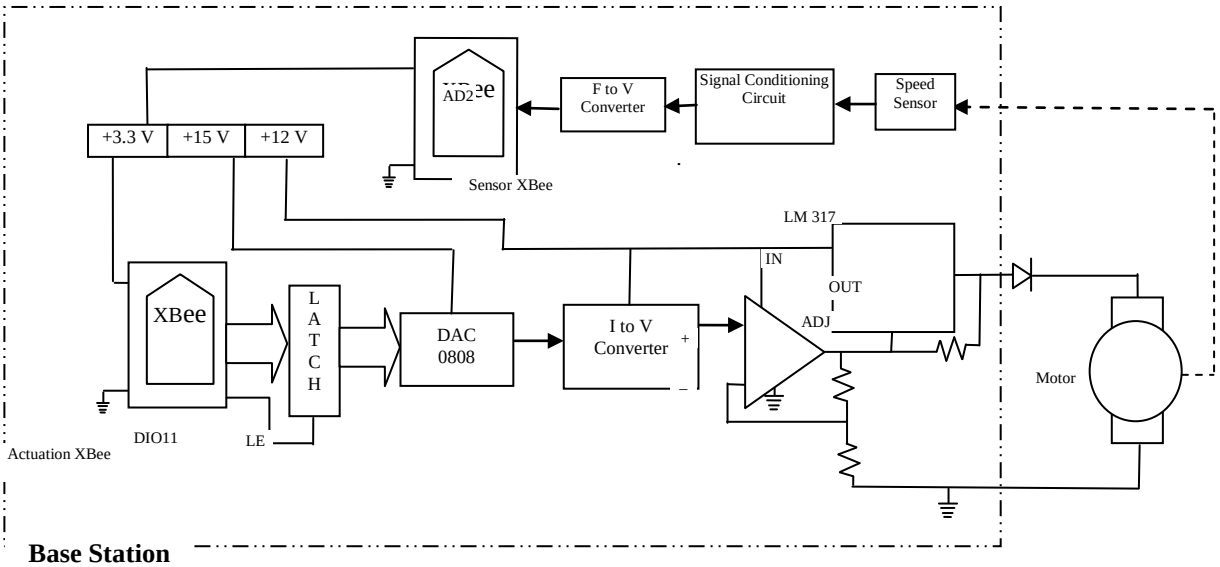

Base Station

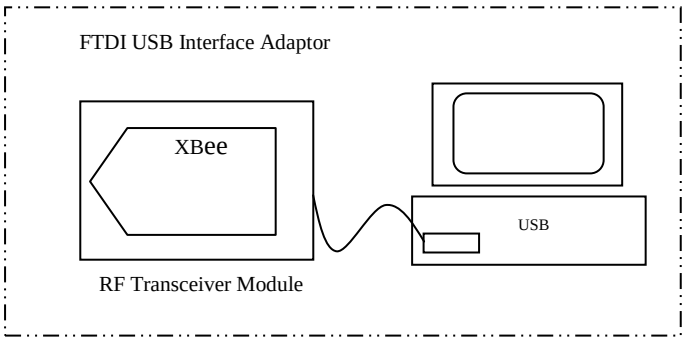

Fig 1 : System Architecture

V. CONTROL METHODOLOGY

The configuration of the Remote Node XBee(s) is done with the XCTU software. Both the Xbee chips are configured as End Devices to function in the API mode. The AD2 input (ADC enabled) of the Sensor XBee has been used to acquire the motor speed signal (pin 18) and the IO sampling rate is set at one second. The DIO pins of the Actuation Xbee are configured as digital outputs. Once configured both the XBee chips are allowed to join the network so that they have the same operating PAN ID. To ensure this the Join Notification and Channel Verification must be enabled for both the Xbee chips.

The sampling rate enables periodic sampling and once the value is set the sensor signal is sampled and transmitted once in every sampling period. This configuration is done by setting parameter IR of the Sensor Node XBee to the appropriate hex value of the desired sampling period in milliseconds. The sensor data is transmitted by the Xbee in API format (API frame type 92 : IO Data Sample Rx Indicator) with the data coded in “Samples” variable (2 bytes) part of the frame. The analog value at the AD2 input pin is converted to 10-bit digital value by the internal ADC of the XBee chip. The maximum analog voltage that can be sensed being 1.2 V, the circuit components have been duly designed to match this requirement.

The control signal is sent from the base station to the Actuation Node Xbee in API format (API frame type 17 : Remote AT Command), for which the 16 bit network address (MY) of the Xbee chip is required. This information can be obtained from the Xbee chip immediately after it has joined the network by sending a Transmit Request (API frame type 10) to it. The Xbee responds by sending a Remote Command Response (API frame type 97) which contains its MY. The output of the control algorithm is converted to a digital 8-bit data which must be mapped onto the eight DIO pins of the Actuation Node Xbee. Two ASCII characters identify the DIO pin and the parameter value decides whether that pin is to be made high or low. (Refer Table 1). A ninth line, DIO11 has been used to enable the output of the octal latch as required, thus eliminating the need for any additional processor.

The signal processing circuits convert the digital data to the necessary analog signal for use by the actuator.

Table 1 : Data Coding in API frame type 17

DIO pin	AT Command in ASCII	HEX Value for the AT command		AT Command Data (HEX) to make		Used for
				Pin low	Pin high	
DIO0	D0	44	30	04	05	Control signal
DIO1	D1	44	31	04	05	
DIO2	D2	44	32	04	05	
DIO3	D3	44	33	04	05	
DIO4	D4	44	34	04	05	
DIO5	D5	44	35	04	05	
DIO6	D6	44	36	04	05	
DIO7	D7	44	37	04	05	
DIO11	P1	50	31	04	05	Hand-shaking

The analog-to-digital conversion of the analog value inside the XBee is an important factor in control accuracy. This being a 10-bit conversion, each bit represents a voltage of 1.172 mv, which corresponds to 0.03 rpm. This translates to a calculated accuracy of ± 0.1 % or better.

VI. RESULTS

The variation of speed with varying armature voltage is shown in Table 2. The data shown is the average of multiple runs. The results indicate conformance with the voltage - rpm characteristics of the motor (Fig 2).

Table 2: Experimental Observations

Voltage across the motor terminals (Volt)	No. of Rotations	Time Taken (Sec)	R.P.M
2	10	86.22	6.96
4	10	56.04	10.71
6	10	43.11	13.92
8	10	36.75	16.33
10	10	25.23	23.78
12	10	24.54	24.45

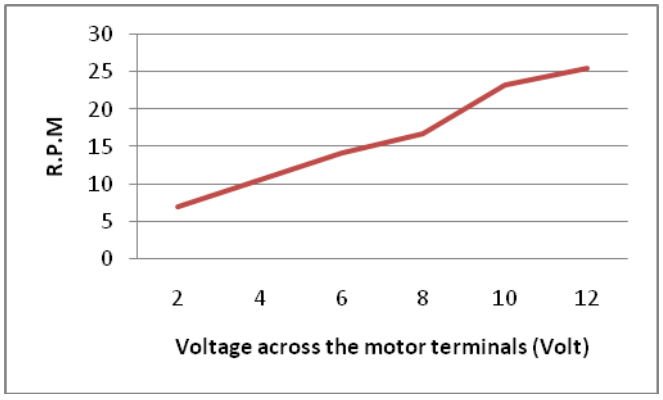

Fig 2 : Voltage – Rpm Motor Characteristics

VII. CONCLUSION

In this work the speed control of the dc motor has been implemented in closed loop. The motor used was a 12 Vdc Motor but this scheme can be applied to higher rated motors simply by increasing the power handling capability of the associated devices. The wireless methodology adopted can be seamlessly used to control other types of final control elements as well. By taking advantage of the processing features of the RF transceiver, the

necessity of a micro-controller has been done away with – thereby substantially reducing the power requirements of the Remote Node. Moreover, advanced control algorithms can be easily implemented in the Base Station PC. Hence this work can be considered as a stepping stone to build robust but low cost schemes for wireless control of end devices in feedback loops.

REFERENCE

[1] F. L. LEWIS, *Wireless Sensor Network, Smart Environments: Technologies, Protocols, and Applications ed. D.J. Cook and S.K. Das, John Wiley, New York, 2004.*

[2] John A. Stankovic, *Department of Computer Science, University of Virginia, Wireless Sensor Networks*

[3] Sukhjit Singh, Neha Sharma, *Research Paper on Drip Irrigation Management using wireless sensors , IRACST – International Journal of Computer Networks and Wireless Communications (IJCNWC), ISSN: 2250- 3501,Vol.2, No4, August 2012*

[4] R. Sengupta, S. Dasgupta, *Design and Development of a Low Cost Scheme for Wireless Speed Control of a DC Motor using PWM, ISSN- 2277-1956, International Journal of Electronics and Computer Science Engineering*

[5] XBee OEM RF Modules by *Digi International Firmware version: 8x0x XBee DigiMesh 2.4*

[6] A. Willing, K. Matheus and A.Wolisz, *Wireless technology in industrial networks , Proceedings of IEEE, vol. 93, no.6, pp. 1130-1151, 2005.*

[7] Akyildiz. I.F, Varun. M.C, Akan. O.B and Su. W, *Wireless sensor networks: A survey Revisited, Computer networks Journal Elsevier, 2006.*

[8] Baggio A (2005), *Wireless sensor networks in precision agriculture,. In: On-line Proc. of the Workshop on Real- World Wireless Sensor Networks, pp. 50-51.*

[9] W. Zhang, G. Kantor, and S. Singh, *Integrated wireless sensor/actuator networks in an agricultural application, in Proc. ACM Conf. on Embed.Net. Sens. Sys. (SenSys), Nov. 2004, p. 317, Baltimore, USA.*

[10] D. Vishnu Vardhan, K. Soundara Rajan, Y. Narasimha Murthy, *Design and Development of Low Power Wireless Sensor System for Measurement and Monitoring of Bio-Medical Parameters, International Journal of Engineering Research (ISSN : 2319-6890)July 2013.*

[11] G.Ahalya et al., *Development of Coal Mine Safety Systems using Wireless Sensor Networks, ISSN: 2250-3676, International Journal of Engineering Science & Advanced Technology] Volume-3, Issue-3, 74-78*

[12] Baggio et al., *Towards Precision Agriculture: Building a Soil Wetness Multi-Hop WSN from First Principles, Ecosense, Belgrade, April 2011.*

[13] Gs Gupta, SC Mukhopadhyay, M. Sutherland, S. Demidenko, *Wireless Sensor Network for Selective Activity Monitoring in a home for the Elderly, Proceedings of 2007 IEEE IMTC conference, Poland, Warsaw 2007,1(3):1-6.*

[14] Manijeh Keshtgari1, Amene Deljoo2, *Wireless Sensor Network Solution for Precision Agriculture Based on ZigBee Technology, Wireless Sensor Network, 2012, 4, 25-30 doi:10.4236/wsn.2012.41004 Published Online January 2012 (http://www.SciRP.org/journal/wsn)*

[15] Callaway, E.H., *Wireless sensor networks: architectures and protocols, Auerbach Publications: New York, NY, USA, 2004*

OBJECT IDENTIFICATION AND COUNTING BASED ON FOREGROUND DETECTION USING MORPHOLOGY IN DYNAMIC TEXTURE SCENES

Venkata Raviteja.M[1], Riyazuddin.K[2]

[1]*M.Tech Scholar, E.C.E, AITS, Rajampet, Andhra Pradesh, (India)*

[2]*Assistant Professor, E.C.E, AITS, Rajampet, Andhra Pradesh, (India)*

ABSTRACT

Background subtraction may be a very fashionable approach for police work moving objects from a still scene. For this, most of previous ways depend upon the belief that the background is static over short time periods. To adopt a clustering-based feature, referred to as fuzzy color bar chart (FCH). it's a capability of greatly attenuating color variations generated by background motions whereas still light moving objects. Background subtraction may be a procedure vision method of extracting foreground objects during a specific scene. A foreground object are often delineate as Associate in Nursing object of attention that helps in reducing the number data} to be processed likewise as offer necessary information to the task into account.

Key words: Background Subtraction, Fuzzy colour Histogram, Object Tracking

I. INTRODUCTION

Background subtraction, conjointly called Foreground Detection, may be a technique within the fields of image process associated pc vision whereby an image's foreground is extracted for additional process (object recognition etc.). distinctive moving objects from a video sequence may be a basic and vital task in several computer-vision applications. a typical approach is to perform background subtraction, that identifies moving objects from the portion of a video frame that differs considerably from a background model. There area unit several challenges in developing an honest background subtraction rule. First, it should be sturdy against changes in illumination. Second, it ought to avoid police work non-stationary background objects like moving leaves, rain, snow, and shadows forged by moving objects. Finally, its internal background model ought to react quickly to changes in background like beginning and stopping of vehicles. Our analysis began with a comparison of varied background subtraction algorithms for police work moving vehicles and pedestrians in urban traffic video sequences (Cheung and Kamath 2004). we have a tendency to thought-about approaches variable from straightforward techniques like frame differencing and reconciling median filtering, to a lot of refined probabilistic modeling techniques. whereas sophisticated techniques typically turn out superior performance, our experiments show that straightforward techniques like reconciling median filtering will turn out sensible results with abundant lower process complexness. usually associate image's regions of interest area unit objects (humans, cars, text etc.) in its foreground. once the stage of image preprocessing (which could embody image denoising, post process like morphology etc.) object localisation is needed which can create use of this method. Background subtraction may be a wide used approach for police work moving objects in videos from static cameras. The principle within the approach is that of police work the moving objects from the

distinction between the present frame and a system, typically known as “background image”, or “background model”. Background subtraction is generally done if the image in question may be a a part of a video stream. Background subtraction provides necessary cues for varied applications in pc vision, as an example police investigation chase or human poses estimation. However, background subtraction is usually supported a static background hypothesis that is usually not applicable in real environments. With indoor scenes, reflections or animated pictures on screens result in background changes. in an exceedingly same manner, thanks to wind, rain or illumination changes brought by weather, static backgrounds strategies have difficulties with outside scenes **Fuzzy Membership Based Local Histogram Features.** In Our Project, color bar chart is viewed as a color distribution from the chance viewpoint. Given a color house containing color bins, the colour bar chart of image containing pixels is delineated as , wherever is that the chance of a constituent within the image happiness to the th color bin, and is that the total range of pixels within the th color bin. per the full applied mathematics, is outlined as follows:

$$\mathbf{h_i}=\sum_{j=1}^{N}\mu ij\mathbf{Pj}=\frac{1}{N}\sum_{j=1}^{N}\mu ij$$

Where Pj is that the chance of a pel hand-picked from image I being the jth pixel, that is 1/N , and Pi/j is that the chance of the chose nth pixel happiness to the ith color bin. With in the context of CCH, is outlined as

In the context of CCH, is outlined asWhere Pj is that the chance of a pel hand-picked from image I being the jth pixel, that is 1/N , and Pi/j is that the chance of the chose nth pixel happiness to the ith color bin. within the context of CCH, is outlined as

In the context of CCH, is outlined as

$$\mathbf{P_{i|j}}=\begin{cases}1, if\ the\ jth\ pixel\ is\ quantized\ into\ the\ jth\ color\ bin\\ 0, otherwise\end{cases}$$

This definition ends up in the boundary issue of CCH such the bar chart might bear abrupt changes albeit color variations are literally little. This reveals the explanation why the CCH is sensitive to hissing interference like illumination changes and division errors. The projected FCH primarily modifies chance Pi|j as follows. rather than victimisation the chance Pi|j, we tend to think about every of the N components in image I being associated with all the colour bins via fuzzy-set membership operate such the degree of “belongingness” or “association” of the th component to the ith color bin is decided by distributing the membership worth of the jth pixel, µij to the ith color bin.

1.1 Definition (Fuzzy Color Histogram)

The fuzzy color bar chart (FCH) of image I may be expressed asF(I)=[f1,f2, f3,..... fn], where

$$f_i=\sum_{j=1}^{N}\mu ij\mathbf{Pj}=\frac{1}{N}\sum_{j=1}^{N}\mu ij$$

has been outlined in (1), and is that the membership worth of fifteenth element within the th color bin. In distinction with CCH, our FCH considers not solely the similarity totally different|of various} colours from different bins however conjointly the unsimilarity of these colours assigned to constant bin. Therefore, FCH effectively alleviates the sensitivity to the clamant interference.

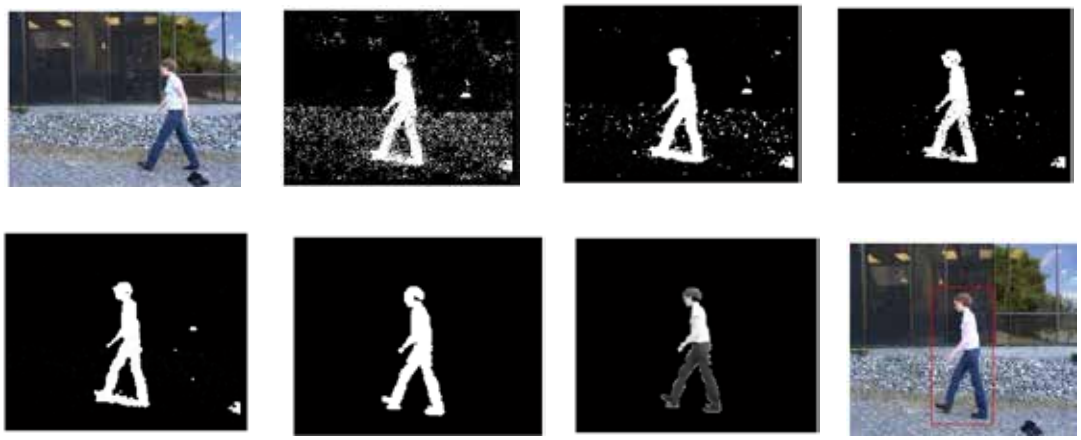

Fuzzy Membership primarily based native bar chart options the thought of mistreatment FCH in a very native manner to get the reliable background model in dynamic texture scenes is impelled by the observation that background motions don't build severe alterations of the scene structure despite the fact that they're cosmopolitan or occur suddenly within the spatiotemporal domain, and color variations yielded by such unsuitable motions will so be with efficiency attenuated by considering native statistics outlined in a very fuzzy manner, i.e., relating to the result of every component price to all or any the colour attributes instead of only 1 matched change the native region (see Fig. 1). Therefore, it's thought that fuzzy membership primarily based native histograms pave the way for sturdy background subtraction in dynamic texture scenes. during this section, we tend to summarize the FCH model [12] and analyze the properties associated with background subtraction in dynamic texture scenes.

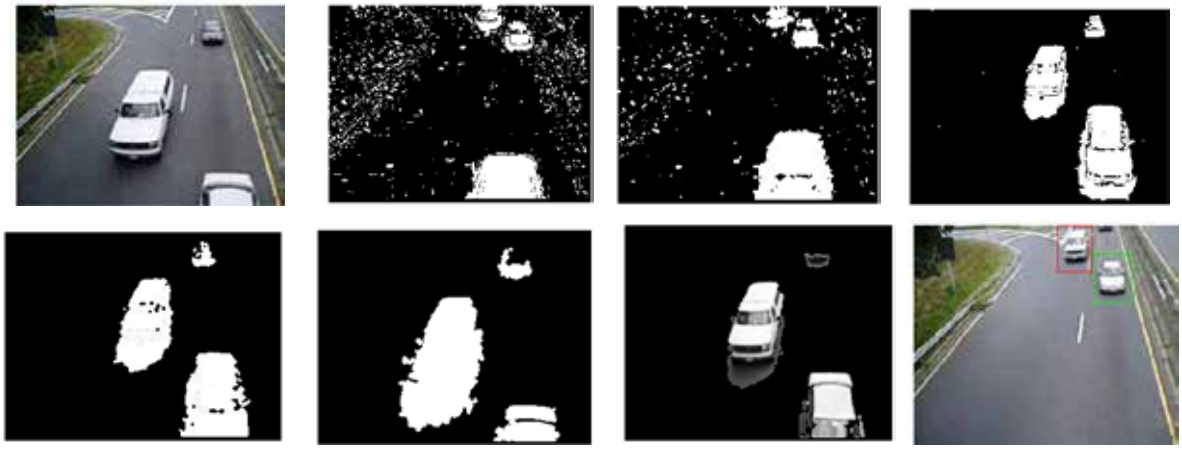

II. BACKGROUND SUBTRACTION WITH LOCAL FCH FEATURES

In this subdivision, we tend to describe the procedure of background subtraction supported our native FCH options. To classify a given picture element into either background or moving objects within the current frame, we tend to initial compare the ascertained FCH vector with the model FCH vector revived by the web update as expressed in (6):

$$Bj(k) = \begin{cases} 1, & \text{if } S(Fj(k), F\hat{}j(k)) \\ 0, & \text{otherwise} \end{cases} > \tau$$

Where Bj(k)=1 denotes that the th element within the th video frame is set because the background whereas the corresponding element belongs to moving objects if.B(j,k)= 0. τ may be a thresholding price starting from zero

to one. The similarity live employed in (6), that adopts normalized bar graph intersection for easy computation, is outlined as follows:

$$s(Fj(K), F\hat{}j(K)) = \frac{\sum_{i=1}^{c} \min[fk, f\hat{}k]}{\max[\sum_{i=1}^{c} fk, \sum_{i=1}^{c} f\hat{}k]}$$

Where denotes the background model of the th constituent position within the th video frame, outlined in (8). Note that the other metric (e.g., trigonometric function similarity, Chi-square, etc.) may be used for this similarity live while not important performance drop. so as to take care of the reliable background model in dynamic texture scenes, we want to update it at every constituent position in an internet manner as follows:

$$F\hat{}_j(k) = (1-\alpha).F\hat{}_j(k-1) + \alpha \, . \, F_j(k) \, , \, k \geq 1$$

Where $F\hat{}_j(0) = F_j(0) \, . \, \alpha \, \mathcal{E}[0 \, ,1]$ is the learning rate. Note that the larger denotes that native FCH options presently discovered powerfully have an effect on to make the background model. By doing this, the background model is adaptively updated. For the sake of completeness, the most steps of the planned technique square measure summarized in formula one.

III. ALGORITHM 1: BACKGROUND SUBTRACTION USING LOCAL FCH FEATURES

Step-1: Construct a membership matrix exploitation fuzzy c-means clustring supported (3) and (4) (conducted offline solely once).

Step-2: Quantize RGB colours of every constituent at the kth video frame into one in every of m bar chart bins(e.g., rth bin wherever r = one,2,.....m).

Step-3: notice the membership worth uir at every constituent position (i=1,2,...c).

Step-4: work out native FCH options exploitation (5) at every constituent position of the kth video frame.

Step-5: Classify every constituent into background or not supported (6).

Step-6: Update the background model using(8).

Step-7: return to step a pair of till the input is terminated (k=k+1).

IV. CONCLUSION

In this paper, we introduce a novel descriptor on representing Background subtraction for dynamic texture using fuzzy c -means clustering algorithm, called fuzzy colour histogram (FCH).Based on extensive experimental results, our FCH is less sensitive and more robust than CCH (Conventional colour histogram) on dealing with illumination changes such as lighting intensity changes, region-of-interest background subtraction, and possibly other uncovered aspects in new applications. Finally, exploiting FCH into other image processing frame- works and even extending similar soft clustering approach to other low-level visual features (e.g., shape, texture, etc.) are also recommended

REFERENCES

[1] M. Heikkila and M. Pietikainen, “A Texture-Based Method for Modeling the Background and Detecting Moving Objects,” IEEE Trans. PAMI, vol. 28, no. 4, pp. 657-662, 2006.

[2] K. Kim, T.H. Chalidabhongse, D. Harwood and L. Davis, “Real-time foreground-background segmentation using codebook model,” Elsevier Real-Time Imaging, vol. 11, pp. 172-185, 2005.

[3] B. Klare and S. Sarkar, "Background subtraction in varying illuminations using an ensemble based on an enlarged feature set," IEEE Conf. CVPR Workshops, pp. 66 – 73, 2009.

[4] P. KaewTraKulPong and R. Bowden, "An Improved Adaptive Background Mixture Model for Real-time Tracking with Shadow Detection," Proc. 2nd European Workshop on Advanced Video Based Surveillance Systems, 2001.

[5] S. Jabri, Z. Duric, H. Wechsler, and A. Rosenfeld, "Detection and Location of People in Video Images Using Adaptive Fusion of Color and Edge Information," Proc. IEEE Int'l Conf. Pattern Recognition, vol. 4, pp. 627-630, 2000.

[6] P. KaewTraKulPong and R. Bowden, "An Improved Adaptive Background Mixture Model for Real-time Tracking with Shadow Detection," Proc. 2nd European Workshop on Advanced Video Based Surveillance Systems, 2001.

[7] S. Jabri, Z. Duric, H. Wechsler, and A. Rosenfeld, "Detection and Location of People in Video Images Using Adaptive Fusion of Color and Edge Information," Proc. IEEE Int'l Conf. Pattern Recognition, vol. 4, pp. 627-630, 2000.

[8] M. Karaman, L. Goldmann, D. Yu and T. Sikora, "Comparison of Static Background Segmentation Methods," Proc. SPIE, vol. 5960, pp. 2140-2151, 2005.

[9] F. El Baf, T. Bouwmans and B. Vachon, "Foreground Detection Using the Choquet Integral," IEEE Ninth Int'l WIAMIS, pp. 187-190, 2008.

BIOGRAPHICAL NOTES

Mr. M. Venkata Ravi Teja is presently pursuing M. Tech. final year in Electronics and Communication Engineering Department (Specialization in Digital Electronics Communication Systems) from A.I.T.S Rajampet, Andhra Pradesh, India.

Mr. K. Riyazuddin is working as a Assistant Professor in Electronics and Communication Engineering Department, A.I.T.S Rajampet, Andhra Pradesh, India.

PSEUDO-DYNAMIC ANALYSIS OF SLOPE

Nipa Chanda

Ph.D Scholar, Department of civil engineering, NIT Agartala,(India)

ABSTRACT

Analysis of slope under seismic loading condition is very much important. Numerous methods have been developed like limit equilibrium method, finite element method, stress deformation analysis, etc. to analyse stability of slopes under seismic conditions. Although, different methods are available to analyse the stability of slopes under both the static and seismic conditions, but the complete solution for the seismic stability of slopes is still an important finding. In the present work an attempt is made here to analyse the stability of slope considering linear wedge failure under pseudo-dynamic condition using limit equilibrium method, which can be used for the design of slope. The results are plotted in non-dimensional charts.

Keywords: Pseudo-dynamic method, stability number

I. INTRODUCTION

Analysis of slopes under seismic condition is an important finding for researchers and engineers. Numerous methods have been developed like limit equilibrium method, finite element method, stress deformation analysis, etc. to analyse stability of slopes under seismic conditions. Classical works to analyse slope under static condition were carried out by researchers like Taylor (1937, 1948) for translation failure of slope on a planar failure surface, the ordinary method of slices by Fellenius (1936) and Bishop's modified method given by Bishop (1955) for circular and log spiral failure surfaces are well understood. Non-homogeneous anisotropic soils with non-circular failure surfaces was analysed by Morgenstern and Price (1965), Spencer (1967), Janbu (1973), Chowdhury (1978) and Zhu et al. (2003). Using pseudo-static model slopes has been further investigated by Terzaghi (1950), Newmark (1965), Seed (1966, 1968), Sarma (1975), Kramerand Smith (1997), Rathje and Bray (1999, 2000), Loukidis et al. (2003), Wartman et al. (2003, 2005). In this present work, a planer failure surface passing through the toe is assumed for a homogeneous soil and by using limiting equilibrium approachstability number of any generalized slope under seismic condition is determined. Acceleration coefficients both in the horizontal and vertical directions are considered in the analysis with a variation of parameters like slope angle, soil friction angle.

II. METHOD OF ANALYSIS

Consider a slope of c-ϕ soil of height H and slope angle i as shown in Fig.1. Seismic inertia forces acting on the slope are $Q_h(t)$ in the horizontal direction and $Q_v(t)$ in vertical direction. AB is the planar failure wedge inclined at an angle α with the horizontal. R is the reaction acting on failure wedge at an angle $\phi_m$with the normal of the failure wedge. $C=c_mL$ is the mobilized cohesion acting along the face AB (length L) and $\phi_m$is the mobilised internal friction angle.

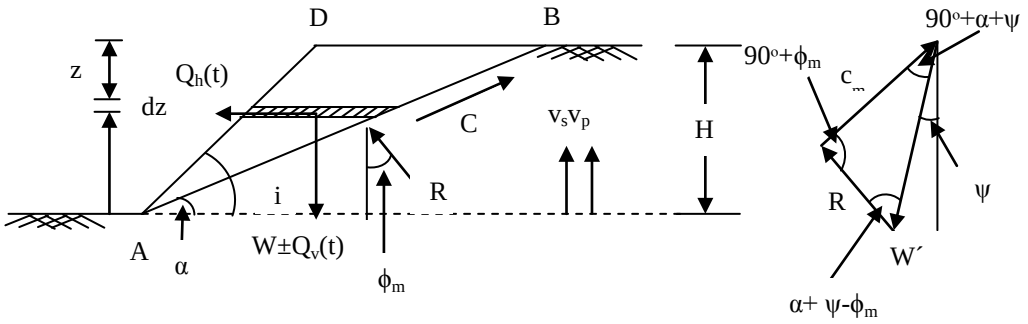

a. Forces acting on the failure wedge

b. Force triangle

Fig.1.Failure mechanism of the soil wedge

Weight of the wedge:

$$W = \frac{g' H^2 (\cot a - \cot i)}{2} \quad (1)$$

The mass of a thin element of wedge at depth z of thickness dz is given by:

$$m(z) = \frac{g'}{g} (\cot a - \cot i)' (H - z)' dz \quad (2)$$

For a sinusoidal base shaking subjected to both horizontal and vertical earthquake acceleration with amplitude $k_h$gand k_vg , the horizontal and vertical acceleration respectively at any depth z below the ground surface at time 't' can be expressed as:

$$a_h(z,t) = k_h' \sin w\left(t - \frac{H - z}{V_s}\right)$$

$$(3)\ a_v(z,t) = k_v' \sin w\left(t - \frac{H - z}{V_p}\right)$$

(4)Therefore, total horizontal inertia force and vertical inertia force acting on the failure wedge are: $Q_h(t) = \int_0^H m(z)' a_h(z,t)$

$$(5)\ Q_v(t) = \int_0^H m(z)' a_v(z,t)$$

(6)

The resultant weight which makes an angle ψ' with vertical and is given as:

$$\psi' = \tan^{-1}\frac{k_h}{(1 \pm k_v)}$$

(7)From Fig.1b using sine rule:

$$\frac{W'}{\sin(90^\circ + \phi_m)} = \frac{C_m}{\sin(\alpha + \psi' - \phi_m)} = \frac{R}{\sin(90^\circ - \alpha - \psi')}$$

(8)Solving Eq.8 we get:

$$S_n = \frac{c_m}{\gamma H} = \frac{\sin\alpha \sin(\alpha + \beta - \phi_m)(\cot\alpha - \cot i)}{2\cos\phi_m}\sqrt{\left[1 \pm \frac{hk_v}{H\pi^2}\left\{2\pi\cos\omega\varepsilon + \frac{h}{H}(\sin\omega\varepsilon - \sin\omega t)\right\} + \left\{\frac{l^2k_h^2}{4\pi^4H^2}\left\{2\pi\cos\omega\chi + \frac{l}{H}(\sin\omega\chi - \sin\omega t)\right\}^2 + \left\{\frac{h^2k_v^2}{4\pi^4H^2}\left\{2\pi\cos\omega\varepsilon + \frac{h}{H}(\sin\omega\varepsilon - \sin\omega t)\right\}^2\right\}\right]^{\frac{1}{2}}} \quad (9)$$

Where, $\varepsilon = t - \frac{H}{V_p}, \chi = t - \frac{H}{V_s}$

III. RESULT AND DISCUSSION

3.1 Stability Number

Stability number for different value of i and ϕ_m are presented in tabular form.

Table 1 Stability Number of slope under pseudo-dynamic condition at different inclination and soil friction angle

k_h=0, k_v=0					K_h=0.1, K_v=0				
i	ϕ=10°	ϕ=20°	ϕ=30°	ϕ=40°	i	ϕ=10°	ϕ=20°	ϕ=30°	ϕ=40°
20°	0.011				20°	0.028	0.00387		

30°	0.031	0.01			30°	0.05	0.02	0.003	0.002
40°	0.053	0.02	0.007		40°	0.075	0.04	0.017	0.003
50°	0.077	0.05	0.023	0.006	50°	0.1	0.07	0.037	0.016
60°	0.105	0.07	0.045	0.023	60°	0.128	0.09	0.063	0.037
70°	0.135	0.1	0.072	0.046	70°	0.16	0.12	0.093	0.066
80°	0.169	0.13	0.105	0.077	80°	0.195	0.16	0.128	0.1
90°	0.21	0.17	0.144	0.116	90°	0.236	0.2	0.171	0.143
K_h=0.1, K_v=0.05					K_h=0.1, K_v=0.1				
i	ϕ=10°	ϕ=20°	ϕ=30°	ϕ=40°	i	ϕ=10°	ϕ=20°	ϕ=30°	ϕ=40°
10°	0.007737				10°	0.008215			
20°	0.027982	0.004116			20°	0.028141	0.004371		
30°	0.05146	0.020058	0.003055		30°	0.05247	0.020172	0.003244	
40°	0.076496	0.041947	0.016928	0.002686	40°	0.078458	0.04277	0.017024	0.002852
50°	0.103362	0.067263	0.038186	0.016055	50°	0.106365	0.068988	0.038936	0.016146
60°	0.132611	0.095808	0.064549	0.038178	60°	0.136757	0.098591	0.066205	0.038928
70°	0.16503	0.128066	0.095791	0.067237	70°	0.17045	0.13207	0.098575	0.068962
80°	0.201721	0.165006	0.132568	0.103308	80°	0.208586	0.170425	0.136713	0.106309
90°	0.244251	0.208157	0.176284	0.147554	90°	0.252795	0.215242	0.182073	0.152168
K_h=0.2, K_v=0					K_h=0.2, K_v=0.1				
i	ϕ=10°	ϕ=20°	ϕ=30°	ϕ=40°	i	ϕ=10°	ϕ=20°	ϕ=30°	ϕ=40°
10°	0.0288	0.0003			10°	0.033	0.0013		
20°	0.051	0.02	2E-04		20°	0.052	0.02	7E-04	
30°	0.075	0.04	0.011	1E-04	30°	0.076	0.04	0.013	6E-04
40°	0.1	0.06	0.031	0.01	40°	0.103	0.06	0.032	0.011
50°	0.126	0.09	0.056	0.03	50°	0.132	0.09	0.057	0.03
60°	0.155	0.12	0.084	0.056	60°	0.163	0.12	0.087	0.057
70°	0.187	0.15	0.117	0.088	70°	0.197	0.16	0.122	0.091
80°	0.223	0.19	0.155	0.126	80°	0.236	0.2	0.163	0.132
90°	0.264	0.23	0.199	0.172	90°	0.281	0.24	0.21	0.181
K_h=0.2, K_v=0.2									
i	ϕ=10°	ϕ=20°	ϕ=30°	ϕ=40°					
10°	0.0373	0.00325							
20°	0.053	0.02	0.002						
30°	0.078	0.04	0.015	0.001					
40°	0.106	0.06	0.033	0.013					
50°	0.137	0.09	0.058	0.032					
60°	0.17	0.13	0.09	0.058					
70°	0.207	0.16	0.127	0.094					
80°	0.249	0.21	0.17	0.137					
90°	0.297	0.26	0.221	0.19					

3.2 Parametric Study

Stability charts for different values of soil friction angle areplotted below

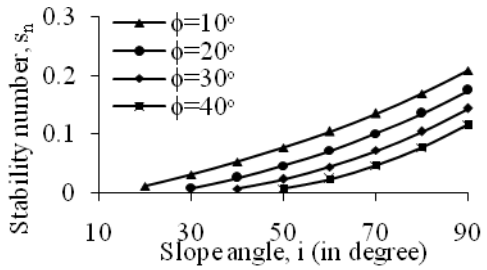

Fig.2.Stability chart for k_h=0, k_w=0

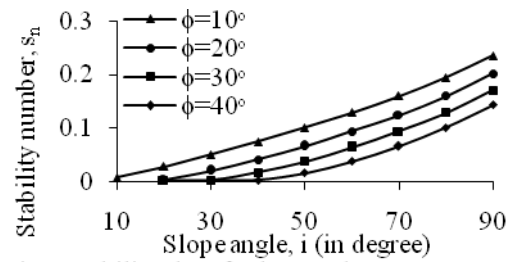

Fig.3.Stability chart for k_h=0.1, k_w=0

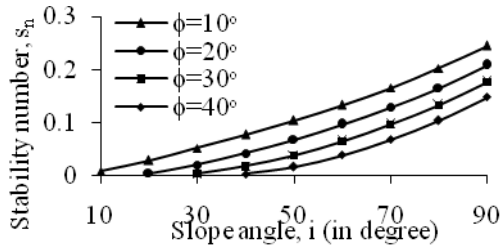

Fig. 4. Stability chart for k_h=0.1, k_v=0.05

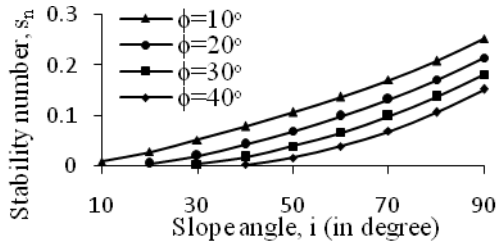

Fig. 5. Stability chart for k_h=0.1, k_v=0.1

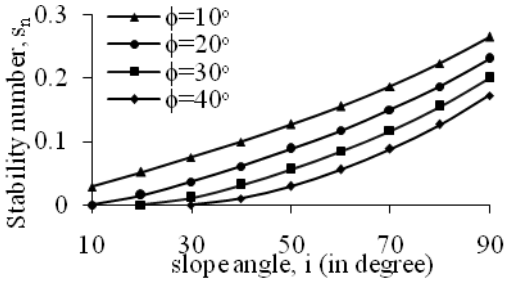

Fig. 6. Stability chart for k_h=0.2, k_v=0

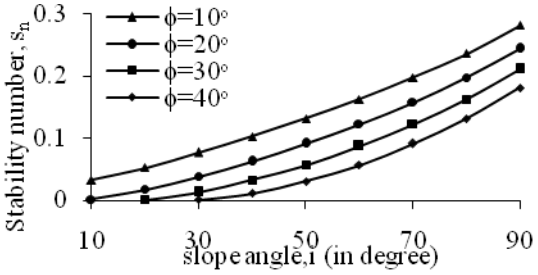

Fig. 7. Stability chart for k_h=0.2, k_v=0.1

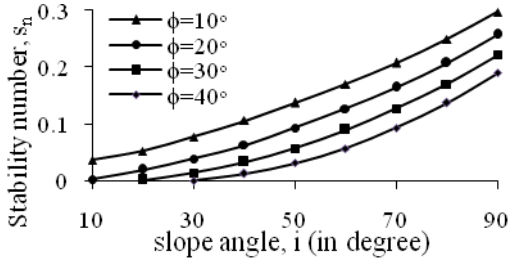

Fig. 8. Stability chart for k_h=0.2, k_v=0.2

Stability charts for different horizontal and vertical acceleration coefficients are plotted below

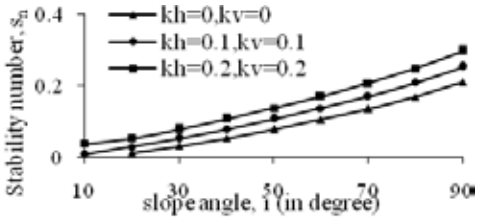

Fig. 9. Stability chart for ϕ=10°

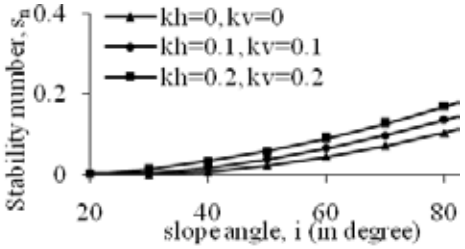

Fig. 10. Stability chart for ϕ=30°

It has been observed that the value of stability number increases due to increase in $k_h$and $k_v$values.

IV. COMPARISON

Stability number obtained in the present study under pseudo-dynamic condition is slightly lesser than the values obtained by Ling et al. (1999) where they considered pseudo-static condition. The comparison is shown in Table 2.

Table 2 Comparison of present study with those obtained by Ling et al. (1999)

ϕ_m	i = 60°, k_h=0.1, k_v=0.05		i = 90°, k_h=0.1, k_v=0.05	
	Ling et al. (1999)	Present study	Ling et al. (1997)	Present study
20°	0.096613	0.095808	0.209887	0.208157
30°	0.065097	0.064549	0.177752	0.176284
40°	0.038512	0.038178	0.148787	0.147554

V. CONCLUSION

In this paper formulation is developed for stability number using pseudo-dynamic approach. Moreover, stability number and stability charts has been given using Pseudo-dynamic method for different values of k_h and k_v and linear interpolation is suggested for any intermediate value.

NOMENCLATURE

a_h , a_v	Amplitude of horizontal and vertical seismic acceleration respectively
g	Acceleration due to gravity.
H	Height of the slope
k_h , k_v	Seismic acceleration coefficient in the horizontal and vertical direction respectively
S_n	Stability number
W	Weight of failure wedge
$Q_h(t)$, $Q_v(t)$	Horizontal and vertical inertia force due to seismic accelerations respectively
t, T	Time (seconds) and period (seconds) of lateral shaking
α	Angle of inclination of the failure surface with the vertical
ϕ	Friction angle of the backfill soil
γ	Unit weight of the soil
c_m	Mobilized cohesion
$\lambda = TV_s$	Wave length of shear wave
$\eta = TV_p$	Wave length of compression wave
$W¢$	Resultant weight, $W¢= \sqrt{Q_h(t)^2 + \{W \pm Q_v(t)\}^2}$

REFERENCES

[1] Taylor, D.W. (1937). “Stability of earth slopes.” Four. Boston Soc. Civil Engrs.,24(3), 197-246.

[2] Taylor, D. W. (1948). Fundamentals of Soil Mechanics. Wiley, New York.

[3] Fellenius, W. (1936). “Calculation of stability of earth dams.” Proc. 2nd Congr. LargeDams,

Washington, 4, 445-462.

[4] Bishop, A.W. (1955). "The use of slip circle in the stability analysis of earth slopes."Geotechnique, 5(1), 7-17.

[5] Morgenstern, N. R., and Price, V. E. (1965). "The analysis of the stability of general slip surfaces."Geotechnique, 15(1), 79-93.

[6] Spencer, E. (1967). "A method of analysis of the stability of embankments assuming parallel interslice forces." Geotechnique, 17(1), 11-26.

[7] Janbu, N. (1973). "Slope stability computations." R. C. Hirschfeld and S. Poulos,eds., John Wiley and Sons, New York, N. Y., 47-86.

[8] Chowdhury, R. N. (1978). Slope Analysis. Elsevier, New York.

[9] Zhu, D. Y., Lee, C. F., and Jiang, H. D. (2003) "Generalised framework of limit equilibrium methods for slope stability analysis." Geotechnique, 53(4), 377-395

[10] Terzaghi, K. (1950). Mechanisms of Land Slides. Engineering Geology (Berkeley) Volume, Geological Society of America.

[11] Newmark, N. (1965). "Effects of earthquakes on dams and embankments."Geotechnique, 15(2), 139-160. 22

[12] Seed, H. B. (1966). "A method for the earthquake resistant design of earth dams." J.Soil Mech. Found Div., ASCE, 92, SM1, 13-41.

[13] Seed, H. B. (1968). "Landslides during earthquakes due to soil liquefaction."Terzaghi Lecture, J. Soil Mech. Found Div., ASCE, 94, SM5, 193-261.

[14] Sarma, S. K. (1975). "Seismic stability of earth dams and embankments."Geotechnique, 25, 743-761.

[15] Kramer, S. L., and Smith, M. W. (1997). "Modified newmark model for seismicdisplacements of compliant slopes". J. Geotech. andGeoenv. Engrg., ASCE, 123(7),
635–644.

[16] H. I. Ling, Y. Mohri, T. Kawabata (1999). "Seismic analysis of sliding wedge: extended Francias-Culmann's analysis." Soil Dynamics and Earthquake Engineering 18 (1999) 387-393.

[17] Deepankar Choudhury, SomdattaBasu and, Jonathan D Bray (2007) "Behaviour of Slopes under Static and Seismic Conditions by Limit Equilibrium Method", M.ASCE.

[18] Dr. K. R. Arora, Soil mechanics and foundation engineering.

[19] Dr. B. C. Punmia, A. K. Jain, A. K. Jain, Soil mechanics and foundations.

[20] GopalRanjan, A S R Rao, Basic and applied soil mechanics.

COMPARATIVE ANALYSIS OF THICKNESS VARIATION OF GATE ON SINGLE & MULTIPLE GATES ORGANIC THIN FILM TRANSISTOR USING SILVACO

Kavery Verma[1], Anket Kumar Verma[2]

[1,2]*Department of Electronics and Communication Engineering J.I.I.T,Noida(India)*

ABSTRACT

In last decades Organic thin film transistors(OTFT) have shown a great improvement on existing technologies and expanded the scope of potentially realizable applications on large-area and flexible devices. This research paper represents the comparative analysis of thickness variation of gate in Single,Dual and Tri-Gate Organic Thin Film Transistor. All the simulations have been carried out using SILVACO TCAD tool. Its performance have analysed on the basis of parameters, which were extracted from its transfer characteristics. The Tri-Gate-OTFT has shown improved electrical performance such as higher on current as compared to single & dual gate OTFT.

Keywords: ATLAS Simulator, Dual Gate Otfts, Organic Thin Film Transistors, SILVACO, Single Gate Otfts, Thickness Variations, Tri Gate Otfts

I.INTRODUCTION

THIN-FILM TRANSISTORS (TFT's) using organic semiconductors as the active material have made an impressive progress in terms of light weight, flexibility, and low cost as compared to other semiconductors.Due to above reasons the imposition of organic thin film transistors (OTFT) are increasingly likely.OTFT will find application, not only in displays, but also to integrate logic circuitry and memory arrays into low cost electronic products such as smart cards, smart price and inventory tags, and large-area sensor arrays.[1,2]. This paper deals with comparative analysis of thickness variation in gate of a single, dual and tri-gate OTFT's structures using 2-D ATLAS simulator. It is observed that Tri-Gate based OTFTs under different configurations outperform the single gate and dual gate ones.

The organisation of paper is as follows. The present section introduces the content of paper.SectionII describes about various gate OTFTs structures.Section III deals with the simulation of thickness variations in gate of all the three types of OTFTs and finally result and discussion is drawn in section IV and conclusion is drawn in section V.

II. OTFT DEVICE DESIGN

An organic field-effect transistor (OTFT) is a Field-effect transistor using an organic semiconductor in its channel.Like MOSFETS, OTFT have symmetrical structures that is source and drain are interchangeable.

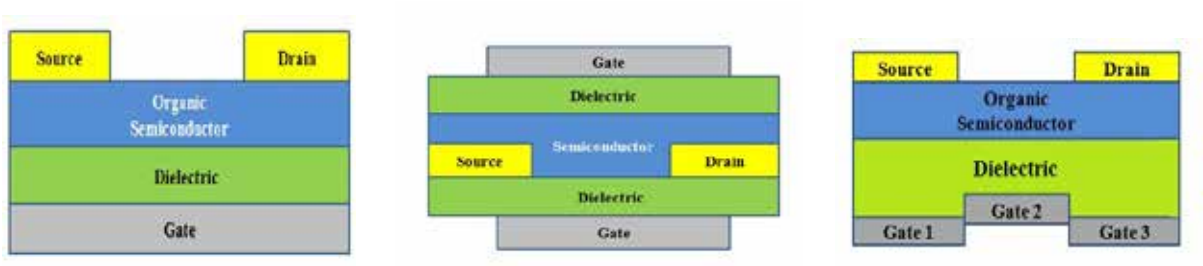

(a) (**b**) (c)

Figure-1.Schematic Cross-Section of OTFT Structures

(A)Single Gate Bottom Gate And Top Contact (SGBGTC) (B) Dual Gate Organic Thin Film Transistors (DGOTFT)(C) Tri Gate Organic Thin Film Transistors (TGOTFT)

Single gate organic thin film transistors (SGOTFT) have been fabricated with various device geometries depending on position of electrodes and gate with respect to semiconductor and dielectric layer. The most commonly used device in single gate geometry is bottom gate with top drain and source electrodes using thermally grown SiO_2 as gate dielectric.This structure is commonly known as bottom gate top contact(BGTC).However in Dual gate organic thin film transistors (DGOTFT) the active semiconducting layer is sandwiched between two gate electrodes from which it is electrically isolated by two gate insulator.While in Tri-gate organic thin film transistors (TGOTFT) gates three gate may be of different thickness embedded in the bottom of structure with three different contact area. The fundamental principles of the operation of the dual gate organic thin film transistors (DGOTFT) and Tri-gate organic thin film transistors(TFOTFT) do not differ from that of a common OTFT. In OTFT the charges are induced by the gate potential at the semiconductor/insulator interface forming a conducting channel. The formation of the channel creates a conducting path between the source and drain electrodes.It also screens the gate potential similar to the operation of a plate capacitor.The change in the threshold voltage of the gate depends on the gate bias[3,4].

III. DEVICE SIMULATION

A 2-D ATLAS simulator of Silvaco Company is used as a semiconductor simulator. The simulation was carried out on three structures: 1)Single gate BGTC, 2) Dual gate OTFT and 3) Tri gate OTFT. We have used an active layer of pentacene with 50-nm thickness in SGBGTC & 100-nm thickness in DGOTFT and TGTFT respectively. The gate insulator was assumed to be SiO_2 a dielectric constant of 3.9 and a thickness of 400 nm. This material prevents gate leakage currents, acts as an effective capacitor.Also it allows for the accurate measurement of the electrical performance of the organic semiconducting layer. ATLAS is generally used for silicon devices. Poole–Frenkel mobility model was adapted for various organic devices .It is given by

$$\mu = \mu_0 \exp\left(-\frac{\Delta Ea - \beta\sqrt{E}}{kBT}\right)$$

where ΔE_a *is* zero field activation energy, whose value is around 5–50 meV, and β is the Poole–Frenkel constant, whose value is around 1×10^{-5}–5×10^{-4} eV $(V/cm)^{1/2}$ for pentacene. The value of μ_0, activation energy (ΔE_a), and β are 0.62 $cm^2\ V^{-1}\ s^{-1}$, 0.018eV, and 7.7×10^{-5} eV $(V/cm)^{1/2}$, respectively.The channel length was taken as 20 μm and the channel width was assumed to be 200 μm.While in case of DGOTFT and TGOTFT silicon was taken for gate material. SiO_2 of 100nm thickness was again taken as insulating layer.The source and drain electrodes were taken of gold with 52.5nm thickness.The channel width and length were 800 μm & 100 μm respectively[5,6].

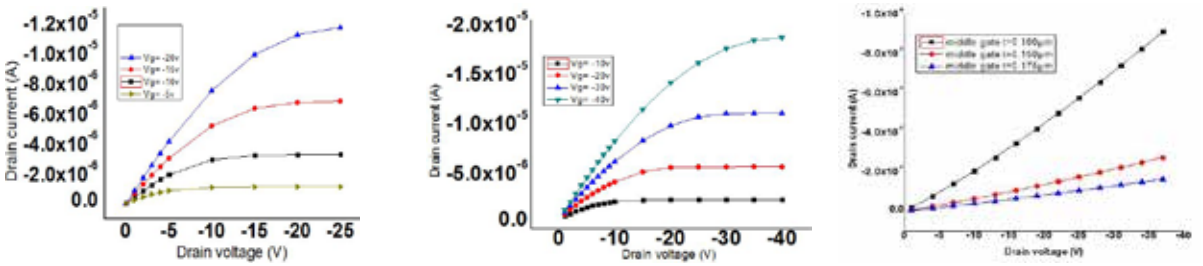

(a) (b) (c)

Figure-2.Output Characteristics A) SGOTFT And B)DGOTFT At Different Gate Voltages C)TGOTFT At Different Mid Gate Thickness Variations.

IV. RESULTS & DISCUSSION

Output characteristics of SGOTFT , DGOTFT and TGOTFT are shown in figure-2 which shows that tri gate structure draws more current compared to the other two gated structure of organic thin film transistor.

Table-I. Extracted Parameters

Parameter	SGOTFT	DGOTFT	TGOTFT
I_{on}/I_{off}	6.68458e+06	1.6383e+13	2.23179e+13

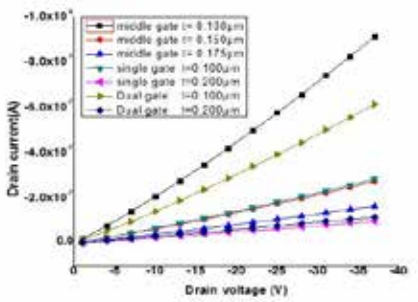

Figure-3 Output Characteristics of Thickness Variations in Gate In All Three Structures.

Figure-3 shows output characteristics of thickness variations in gates from 100nm to 200nm at V_{gs}= -40V(bottom gate in case of DGOTFT and middle gate in case of TGOTFT). Table-1 shows extracted parameters value for both the transistor at 40nm electrode thickness. It has been noted that Tri gate OTFT shows improved switching characteristics (on vs off) compared to earlier transistors. There is decrease in on current with increase in gate width in all three transistors.It consumes far less power than current transistors.

V. CONCLUSION

In this paper performance of SGOTFT,DGOTFT and TGOTFT is analysed by variation of thickness of gate.It can be concluded that tri-gate OTFT has shown superior performance as compared to single gate OTFT such as higher on current which proves to be a better device for switching application.TGOTFT results in higher current due to formation of three conducting channels. Therefore,it can be concluded that Tri-gate is more suitable for applications in large area of electronics.

REFERENCES

[1] Hagen Klauk,David J. Gundlach, and Thomas N. Jackson, " Fast Organic Thin-Film Transistor Circuits", IEEE Electron Device Lett., vol. 20, pp. 289-291, June 1999.

[2] Shradha Saxena, Brijesh Kumar, B. K. Kaushik, Y. S. Negi and G.D.Verma., "Organic Thin Film Transistors: Analytical Modeling and Structures Analysis" Recent Advances in Information Technology (RAIT),pp. 701- 706, Mar. 2012.

[3] G.H.Gelinck, E.van Veenendaal and R. Coehoorn, " Dual-gate organic thin-film transistors" Appl. Phys. Lett., vol.87, 2005.

[4] D. K. Agrahari, J.Singh, P.S.Yadav, et al.,"High Performance Organic Field Effect Transistor with Tri-Gate," Proc. IEEE conf. Intelligent Systems Modeling & Simulation (ISMS), vol.4, pp.627-630, 2013.

[5] J. B. Koo, C. H. Ku, S. C. Lim, et al., "Threshold voltage control of pentacene thin-film transistor with dual-gate structure," J.Info. Display,vol.7, pp. 27-30, 2006.

[6] F. Maddalena, M. Spijkman, J.J Hummelen, D.M de Leeuw, P.W.M Blom, B.de Boer, "Device characteristics of polymer dual-gate field-effect transistor"vol.9,2008.

[7] Chang-Hoon Shim, Fumito Maruoka, and Reiji Hattori, "Structural Analysis on Organic Thin-Film Transistor With Device Simulation "vol. 57,pp. 195-200,Jan.2010.